Structural organization of p62 filaments and the cellular ultrastructure of calcium-rich p62-enwrapped lipid droplet cargo

Author information

Sabrina Berkamp[1#], Lisa jungbluth[1#], Alexandros Katranidis[1#], Siavash Mostafavi[1], Olivera Korculanin[1,5], Peng-Han Lu[2], Lokesh Sharma[3], Lipi Thukral[3,4], Jörg Fitter[1,5], Rafal E. Dunin-Borkowski[2], Carsten Sachse[1,6†]

[1]Ernst-Ruska Centre for Microscopy and Spectroscopy with Electrons, ER-C-3/Structural Biology, Forschungszentrum Jülich, 52425 Jülich, Germany.

[2]Ernst-Ruska Centre for Microscopy and Spectroscopy with Electrons, ER-C-1/Physics of Nanoscale Systems, Forschungszentrum Jülich, 52425 Jülich, Germany

[3]Computational Structural Biology Lab, CSIR-Institute of Genomics and Integrative Biology, Mathura Road, New Delhi 110025, India

[4]Academy of Scientific and Innovative Research (AcSIR), Ghaziabad 201002, India

[5]RWTH Aachen, I.Physikalisches Institut (IA), Aachen, Germany

[6]Department of Biology, Heinrich Heine University, Universitätsstr. 1, 40225 Düsseldorf, Germany.

[#]These authors contributed equally

[†] Correspondence: c.sachse@fz-juelich.de (C.S.)

Keywords: cryo-electron microscopy, helical reconstruction, autophagy, p62/SQSTM1, liquid-liquid phase separation, cryo-electron tomography, correlative light and electron microscopy (CLEM), focused ion beam scanning electron microscopy (FIB-SEM), energy-dispersive X-ray (EDX) spectroscopy, lipid droplets, lipophagy

Abstract

The selective autophagy receptor p62/SQSTM1 (from hereon p62) is known to form higher-order filaments in vitro and to undergo liquid-liquid phase separation when mixed with poly-ubiquitin. We determined the full-length cryo-EM structure of p62 and elucidated a structured double helical filament scaffold composed of the PB1-domain associated with the flexible C-terminal part residing in the lumen and the solvent-accessible major groove. At different pH values and upon binding to soluble LC3, LC3-conjugated membranes and poly-ubiquitin, we observed p62 filament re-arrangements in the form of structural unwinding, disassembly, lateral association and bundling, respectively. In the cellular environment, under conditions of ATG5 knockdown leading to stalled autophagy, we imaged high-contrast layers consisting of p62 oligomers enwrapping lipid droplets by cryogenic electron tomography in cellulo, which we identified as calcium phosphate by compositional spectroscopy analysis. Together, we visualized the cellular ultrastructure of p62 oligomers with high calcium content as a potential intermediate step of autophagy initiation.

Introduction

Autophagy is a conserved cellular process that degrades and recycles cytoplasmic material such as aggregated proteins, damaged organelles and pathogens to maintain intracellular homeostasis (Mizushima et al., 2011; Wen & Klionsky, 2016). While autophagy operates at a basal level for routine maintenance, it can also be activated by stress factors like nutrient deprivation, hypoxia and DNA damage (Kroemer et al., 2010). There are three main autophagy pathways: macroautophagy, microautophagy and chaperone-mediated autophagy. In macroautophagy (from here on simply referred to as autophagy), an autophagosome forms within the cytoplasm to enclose cellular material that is subsequently degraded and recycled after fusing with a lysosome. A series of defined autophagy core machinery complexes mediate the progression of cellular autophagy: Atg1/ULK1 kinase, PI-3 kinase, ATG9 lipid scramblase, the ATG2-ATG18 lipid transfer complex and two ubiquitin-like conjugation systems (Xie & Klionsky, 2007). The recognition of cargo can proceed in a non-selective or in a selective manner by either enclosing the bulk stochastically or through specific binding by selective autophagy receptors, respectively (Y. Feng et al., 2014).

Selective autophagy requires cargo receptors that recognize poly-ubiquitinated cargo and interact with Atg8 family proteins (Kraft et al., 2014; Y.-K. Lee & Lee, 2016). The Atg8 family contains ubiquitin-like proteins: Atg8 in yeast and microtubule-associated protein 1 light chain 3 (LC3) as well as gamma-aminobutyric acid type A receptor-associated protein (GABARAP) in mammals (Shpilka et al., 2011). The conjugation of Atg8 proteins to the lipid membrane is essential for phagophore membrane expansion (Mizushima et al., 2001) and is mediated by two autophagy-specific ubiquitin-like conjugation systems: ATG12-ATG5 and the LC3 conjugation system (Nakatogawa et al., 2009). Selective autophagy receptors, like p62/SQSTM1 (from here on: p62) (Bjørkøy et al., 2005), contain an LC3-interacting region (LIR) motif that facilitates interaction with Atg8 proteins and a ubiquitin-binding domain (Birgisdottir et al., 2013; Rogov et al., 2014). In the meantime, a series of additional autophagy receptors have been identified with LIR motifs as well as ubiquitin binding abilities in order to confer specificity and redundancy in the cargo recognition and removal. For instance, for mitophagy NBR1, optineurin, NDP52 and TAXBP1 have been characterized in addition to p62 (Lazarou et al., 2015). While p62 knock-outs are viable for an organism, long-term benefits of increased p62 levels have been found to promote proteastasis and longevity in response to stress in C.*elegans* (Kumsta et al., 2019).

p62 has a key role in selective autophagy by recognizing poly-ubiquitinated cargo and delivering it to the autophagosome (Bjørkøy et al., 2005). Originally, p62 was

78 described as an interaction partner for tyrosine-protein kinase Lck (Joung et al., 1996),
79 while it was also shown to be involved in multiple pathways including Wnt, Nrf2,
80 mTORC and NF-κB signaling (Puissant et al., 2012). In the NF-κB pathway, p62 can
81 interact with MEKK3, MEK5, aPKCs (Lamark et al., 2003) and tumor necrosis factor
82 receptor associated factor 6 (TRAF6) as a mediator in tumorigenesis (Duran et al.,
83 2011). Moreover, p62 actively promotes the spatio-temporal organization of autophagy
84 downstream effectors such as FIP200 at the cargo site (Turco et al., 2019). p62 is a
85 multi-domain protein with a Phox1 and Bem1p (PB1) domain, followed by a ZZ-domain
86 and an intrinsically disordered region (IDR) up to the C-terminal ubiquitin-binding
87 associated (UBA) domain. The PB1 domain is responsible for p62 polymerization into
88 long flexible filaments (Ciuffa et al., 2015; Jakobi et al., 2020) and was shown to be
89 critical for its function in autophagy as polymerization deficient mutations excluded p62
90 from the autophagosome formation site (Itakura & Mizushima, 2011). The IDR
91 contains several relevant interaction motifs, including the LIR and KEAP1-interacting
92 region (KIR) motif (Komatsu et al., 2010). The C-terminal UBA domain captures poly-
93 ubiquitinated cargo (Ciani et al., 2003). The autophagy receptor NBR1 is structurally
94 the most similar to p62 amongst the autophagy receptors as it is closely evolutionarily
95 related and directly interacts with p62 via its PB1 domain albeit it is unable to form
96 higher-order oligomers or filaments (Jakobi et al., 2020; Kirkin et al., 2009).

97 p62 is a well-studied cargo receptor that recognizes and removes various different
98 cellular cargoes: aggregated proteins in aggrephagy (Bjørkøy et al., 2005; Pankiv et
99 al., 2007), damaged peroxisomes in pexophagy (Zhang et al., 2015) and lipid droplets
100 in lipophagy (L. Wang et al., 2017; Yan et al., 2019). For lipophagy, the size of the
101 removed lipid droplets is smaller than one μm while larger lipid droplets were shown
102 to be predominantly degraded by lipolysis (Schott et al., 2019). At the same time, lipid
103 droplets are a special cargo in the context of autophagy as they can also serve as a
104 direct or indirect lipid source for the growing phagophore mediated by direct contact in
105 addition to the ATG9A vesicles or ATG2 lipid bridges (Dupont et al., 2014; Korfhage
106 et al., 2023; Mailler et al., 2021; Shpilka et al., 2015). Lipid droplets were also found
107 to serve as direct substrates for non-canonical autophagy during prolonged starvation
108 after LC3-conjugation (Omrane et al., 2023).

109 p62 has also been shown to undergo liquid-liquid phase separation (Brangwynne et
110 al., 2009) induced by poly-ubiquitin interaction with multiple polymerized p62 entities
111 in vitro (Sun et al., 2018; Zaffagnini et al., 2018a). However, in vivo, p62 phase
112 separated condensates recruit many autophagy regulators that can affect the mobility
113 of the separated phase and as a result autophagy efficiency. For instance, Keap1

114 over-expression was observed to increase the rigidity of p62 condensates, thus
115 promoting autophagy (Y. Lee et al., 2017). NBR1 enhances p62 condensate formation
116 and poly-ubiquitin affinity (Turco et al., 2021). In addition to binding partners, the
117 oligomeric state of p62 and post-translational modifications can affect the phase
118 separation properties, e.g., as the IDR of p62 harbors the KIR motif that when post-
119 translationally modified has been shown to enhance the interaction with Keap1
120 (Ichimura et al., 2013). The quaternary structural organization of p62 presents another
121 level of regulation for cellular phase separation as phosphorylation of the PB1 domain
122 by PKA was identified and shown to disrupt PB1 domain interactions (Christian et al.,
123 2014).

124 In order to improve our detailed structural understanding of purified p62, we
125 determined the cryo-electron microscopy (cryo-EM) structure of full-length p62. The
126 structure revealed the double helical organization of an N-terminal PB1-domain
127 scaffold while the more poorly resolved partially disordered C-terminal part resided in
128 the lumen and the major groove of the assembly. Binding studies of LC3b and poly-
129 ubiquitin showed that p62 filaments can undergo structural re-arrangements of
130 disassembly or filament bundling, respectively. When p62 filaments were added to
131 LC3b-conjugated membranes, they associate laterally and also unwind their regular
132 helical structures into bubbles at physiological pH. Native ultrastructural imaging of
133 p62-positive structures using cryo-electron tomography (cryo-ET) in ATG5 depleted
134 RPE1 cells revealed stalled intermediate autophagy stages of p62-enwrapped lipid
135 droplets. Interestingly, the surrounding p62 layer had a dark contrast and contained
136 high levels of calcium and phosphorus based on energy-dispersive X-ray
137 spectroscopy analysis (EDX). The high-resolution visualization of p62-enwrapped
138 cargo together with calcium may present an important intermediate state of autophagy
139 initiation.

140 Results

141 p62 forms a double-helical filament with a PB1 scaffold and a flexible C-
142 terminus in the major groove

143 Previously, we determined the three-dimensional (3D) cryo-EM structure of the p62-
144 PB1 domain arranged in a series of different filamentous assemblies (Jakobi et al.,
145 2020). In order to advance our structural understanding of full-length human p62, we
146 optimized the previous preparations of full-length p62 for improved homogeneity. As
147 previous studies suggested an effect of pH on the assembly conditions (Kwon et al.,
148 2018), we compared the preparations at different pHs. Classifications of small cryo-

149 EM test data sets revealed that at pH=6 the majority of the filament classes were
150 helically regular while at pH=8 a large fraction of them were found unwound
151 resembling an open bubble (**Supplementary Fig. 1A**). Therefore, we recorded a full
152 cryo-EM data set at pH=6 revealing long and flexible filaments with a width of
153 approximately 15 nm (**Figure 1A**). Using segmented helical reconstruction (Desfosses
154 et al., 2014; Punjani et al., 2017; Scheres, 2012), we set out to determine the structure
155 of p62 filaments. Due to pitch heterogeneity between 130 and 160 Å (**Figure 1B** and
156 **Supplementary Fig. 1B**), we refined a more homogeneous subset with a 150 Å pitch
157 and 13.6 units per turn (corresponding to 11.0 Å helical rise and a -26.1° helical
158 rotation) including dihedral symmetry and obtained a 3D reconstruction at 4.5 Å global
159 resolution (**Supplementary Fig. 1C-D, Table 1**). Consistent with the class averages,
160 the local resolution varied significantly from a well-defined PB1 domain scaffold at 4.2
161 Å resolution up to over 9 Å for the more flexible regions (**Figure 1C**). The cryo-EM
162 structure revealed a left-handed double-helical filament with two antiparallel strands
163 of PB1 domains in the full-length p62 assembly. The atomic model of the PB1 domain
164 of p62 (PDB: 6TGY) fitted well in the best defined scaffold density supporting β-strand
165 separation (**Figure 1D left**). At lower density thresholds, the ZZ domain envelope
166 emerged connected to the PB1 domain albeit at lower resolution (**Figure 1D right**).
167 The densities of the associated C-terminal domains were weak and poorly resolved
168 presumably due to flexibility with respect to the PB1 strands. Based on our p62
169 filament structure, we expanded the domains to match the PB1 density to the
170 experimentally observed helical symmetry assembly (**Figure 1E**). The resulting p62
171 double helix architecture is built on the scaffold of the PB1 domain generating a major
172 groove that can accommodate the flexible C-terminal part.

173 **Table 1: Cryo-EM structure determination of full-length p62.**

Processing type	Helical segments
Microscope	Talos Arctica 200 keV
Detector	Gatan K3
Magnification	100,000x
Defocus range [μm]	-0.5 to -3.0

Physical pixel size [Å]	1.6778
Total dose [e^-/Å^2]	50
Micrographs	4038
Extraction box size [Å]	503
Overlap [%]	90
Initial no. of segments	1,000,000
Final no. of segments	600,000
Helical symmetry	
Pitch [Å]	150
Rise [Å]	10.985
Rotation [º]	-26.141
Global map resolution (FSC=0.143)/FDR-FSC [Å]	4.5/4.5

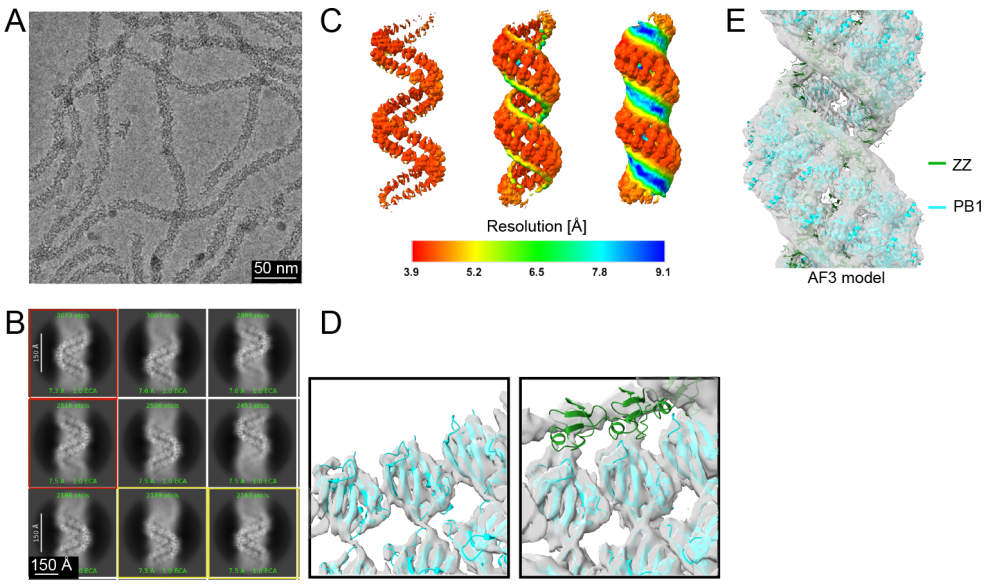

Figure 1: Cryo-EM structure and atomic model of full-length p62 filaments. (A) Representative cryo-micrograph with long and flexible p62 filaments. (B) 2D classes showing well-defined densities of the filamentous scaffold in addition to blur including apparent variation in pitch, with higher helical pitch classes (red frame) and lower helical pitch classes (yellow frame). (C) Three-dimensional density of p62 superimposed with local resolution values showing PB1 domains arranged in a left-handed double helical architecture. The map rendered at different thresholds shows that the PB1 domain is well-resolved (~4.5 Å resolution), the ZZ domain appears as a featureless blob at ~6.5 Å resolution and the remaining C-terminal domains are not well resolved. (D) Left: The atomic model of the PB1 domain fits well into well-defined PB1 density at higher threshold. Right: The atomic model of the ZZ domain of p62 fits in the featureless blobs seen at lower threshold. (E) The atomic model of the helical p62 filament with highlighted PB1 (cyan) and ZZ (green) domains fitted into the filament density displayed at low threshold.

p62 filament interactions with LC3b and ubiquitin

To experimentally study the interactions of p62 filaments with LC3b and ubiquitin, we employed single-particle fluorescence microscopy in total internal reflection fluorescence (TIRF) mode and negative staining EM. We formed p62 filaments at pH=8 and subsequently labeled them at lysine residues with multiple Cy5 dyes (p62 filaments-Cy5) while cyan fluorescent protein (CFP) was fused to LC3b (CFP-LC3b). Consistent with the observed p62 filaments, elongated p62 structures were visible in the Cy5 channel, rather mobile and diffusing above the surface in dilute nM concentrations on the cover slip (**Figure 2A** and **Supplementary Video 1**). Upon addition of equimolar amounts of CFP-LC3b, the same filament became visible in the CFP channel as well (**Figure 2B** and **Supplementary Video 2**) supporting that LC3b

201 was bound to the p62 filaments. Upon addition of GST-4xUbiquitin (GST-4xUb) to the
202 labeled filaments, we observed a rapid and spontaneous formation of μm-sized
203 condensates that displayed minimal mobility (**Figure 2C** and **Supplementary Video**
204 **3**). Interestingly, the subsequent addition of CFP-LC3b to the formed condensates,
205 resulted in the appearance of smaller mobile diffusing fragments (**Figure 2D** and
206 **Supplementary Video 4**).

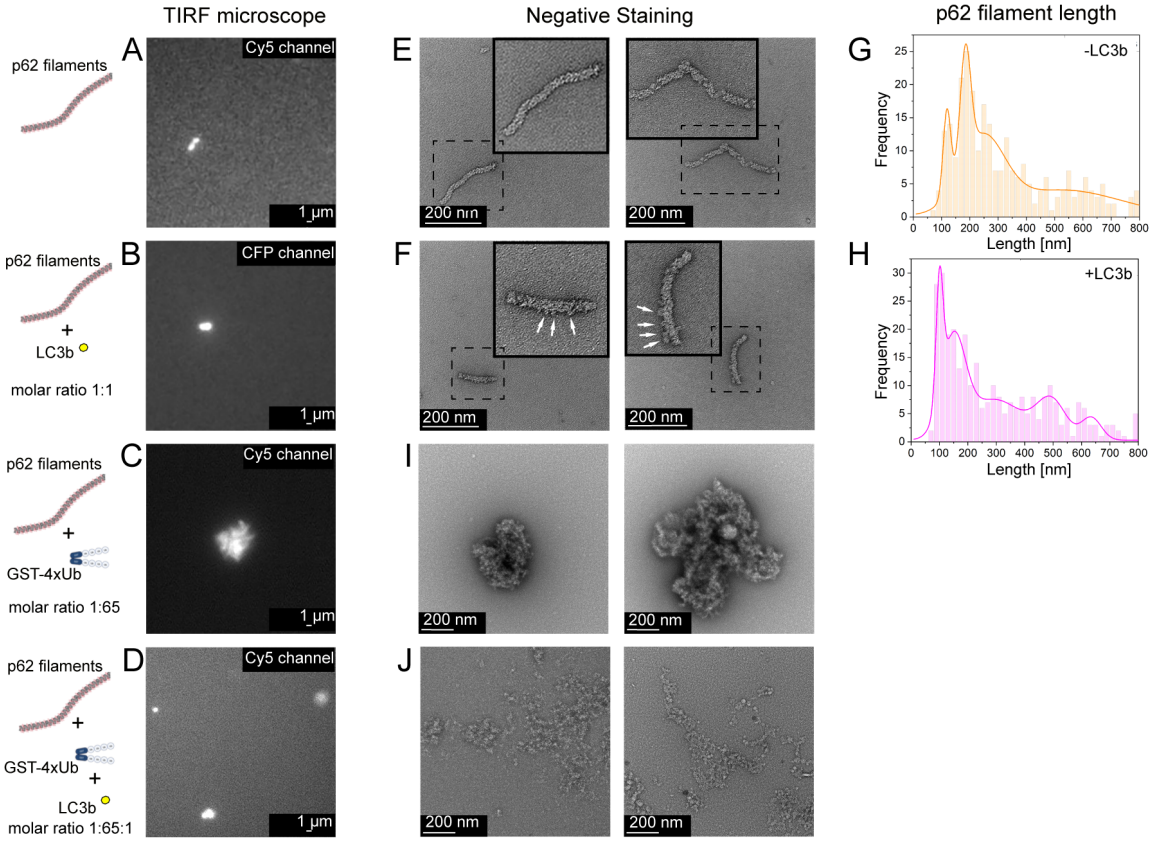

207

208 **Figure 2: LC3b and poly-ubiquitin interactions with p62 filaments visualized by**
209 **single-particle fluorescence and negative staining EM. p62 filament (A) labeled**
210 **with Cy5 on TIRF microscope and (B) in the presence of CFP-LC3b. (C) p62**
211 **condensates forming in the presence of GST4x-ubiquitin (GST4x-Ub). (D) p62**
212 **condensates formed by GST4x-Ub disintegrate after addition of LC3b. (E) Negative**
213 **staining of p62 filaments. Dashed boxes correspond to inset at higher**
214 **magnification. (F) Negative staining of p62 filaments decorated with LC3b (sample**
215 **as in B) (white arrows in inset). Histograms of (G) p62 filament length (H) after**
216 **addition of LC3b. (I) Negative staining of p62 condensates (sample as in D with**
217 **GST4x-Ub). (J) Negative staining of p62 condensates after addition of LC3b (sample**
218 **as in D with GST4x-Ub).**

219 The corresponding p62 filament samples in nM concentration were also imaged by
220 negative staining EM. In the presence of CFP-LC3b, p62 filaments exhibited a
221 distinctive decoration in comparison with the filaments alone (**Figure 2E/F**, white

222 arrows in insets). A quantitative analysis of the filament length distribution revealed a
223 shift towards shorter filaments for CFP-LC3b (**Figure 2G/H**), suggesting that
224 interaction with LC3b induced depolymerization of p62 filaments. Similarly, in the
225 presence of CFP-LC3b, GST-4xUb-induced condensates were disintegrated into
226 smaller substructures (**Figure 2I/J**). In support of previous studies (Sun et al., 2019;
227 Zaffagnini et al., 2018b), our single-particle studies in fluorescence and electron
228 microscopy performed in diluted nM concentration showed that poly-ubiquitinated
229 cargoes induce condensate formation while LC3b can promote disassembly of
230 preformed p62 filaments as well as preformed condensates.

231 In order to molecularly assess the cryo-EM structure and the presented binding
232 experiments, we generated a multimer AI-prediction of p62 using AlphaFold3 (AF3)
233 (Abramson et al., 2024) consisting of ten subunits that formed closed rings mediated
234 by the well-characterized PB1 domain interactions (**Supplementary Fig. 2A**). In an
235 expanded model matching the helical symmetry, the C-terminal UBA domain fits tightly
236 to the major groove next to the PB1 domain that is consistent with the cryo-EM density
237 (**Supplementary Fig. 2B**). When the model is seen in top view, the PB1 domain
238 scaffold and UBA domain are located at the outer rim of the filament while the ZZ
239 domain is located on the inside. Notably, parts of the IDR, including the LIR and KIR
240 binding motifs, are positioned towards the filament's outside, supporting the observed
241 molecular access of p62 interacting partners through the major groove of the filament.
242 To assess the interaction accessibility within the p62 filament in more detail, we
243 generated a second p62 multimer model in the above described way, this time with
244 LC3b known to bind to the LIR motif of p62 (Pankiv et al., 2007). In the resulting model,
245 LC3b is tightly fit in the filament's major groove surface between the PB1 domain and
246 covering the UBA domain (**Supplementary Fig. 2C**). The LIR of p62 is positioned
247 outward and bound in the hydrophobic pocket 1 (HP1) and 2 (HP2) of LC3 in
248 agreement with previously determined X-ray structures (Ichimura et al., 2008). A third
249 p62 AF3-model with bound ubiquitin revealed that ubiquitin also resided in the major
250 groove suggesting a competing mode between LC3b and ubiquitin binding. Together,
251 the AF3-based integrative molecular model of the p62 filament supports the observed
252 accessibility to binding partners of ubiquitin and LC3b while it also provides a
253 molecular framework for the observed opposing higher-order structures of filament
254 bundling and disassembly.

255 p62 filament membrane interactions

256 In order to more closely mimic the cellular conditions, we performed the interaction
257 studies at higher μM concentrations of p62 and investigated the binding of GST-4xUb

258 and LC3b maleimide-conjugated to small unilamellar vesicles (SUVs). Subsequently,
259 we visualized the natively preserved ultrastructures using cryo-ET. To better
260 characterize the fine ultrastructure of p62 filaments on the image level, we recorded
261 tomograms using the Volta phase plate for detailed high-contrast visualization. The
262 resulting 3D tomograms showed 15 nm-wide flexible p62 filaments consistent with
263 repeating pitches of 14 nm along the filament exhibiting regular major groove
264 indentations matching the pH=6 conditions described above (**Figure 3A**). Closer
265 inspection revealed overlapping filaments crossing underneath each other, branching
266 filaments where individual PB1 scaffold strands are adopting a close to 90º bent as
267 well as a cross-over reminiscent of Holliday junctions in double-stranded DNA. Due to
268 the underfocus-induced white halo of phase plate surrounding the filament density, we
269 turned back to conventional cryo-imaging at underfocus and closer to physiological pH
270 7.4 for the subsequent tomograms. Upon addition of GST-4xUb, p62 filaments were
271 found to concentrate locally by forming bundles of parallel filaments supported by
272 filament image segmentations (**Figure 3B**). Bundle formation was accompanied by
273 the formation of μm-sized 3D agglomerates that were often too thick to be imaged by
274 cryo-ET while visible by negative staining EM (**Supplementary Fig. 3**) being
275 consistent with the previous in vitro observations of phase separated p62 bodies (Sun
276 et al., 2019; Zaffagnini et al., 2018b). When we incubated p62 filaments with LC3b-
277 conjugated SUVs, we observed unbound filaments as in the p62-only control in
278 proximity to SUVs as well as SUV bound filaments (**Figure 3C**). When not bound, the
279 p62 exhibited the typical filament appearance with a regular 14 nm pitch and major
280 groove indentations as well as unwound stretches of the high pH=8 p62 sample alone
281 (**Figure 3D**). When p62 filaments were found connected to the SUV density, they were
282 either laterally associated along the membrane of the SUVs or bound through their
283 ends. As in solution, some laterally associated filaments were characterized by
284 densities giving up the regular helical pitch 14 nm repeat giving rise to more open and
285 unwound stretches. The co-incubation of GST-4xUb and LC3b-conjugated SUVs
286 resulted in less dense network of filament bundles in comparison with GST-4xUb alone
287 as well as SUV bound filaments (**Figure 3E**). Together, the cryo-ET visualization of
288 purified p62 revealed the flexible properties of p62 filaments including cross-overs and
289 branching, bundling of parallel p62 filaments in GST-4xUb bound condensates as well
290 as the lateral association of the helical assembly on the surface of LC3b-conjugated
291 membranes.

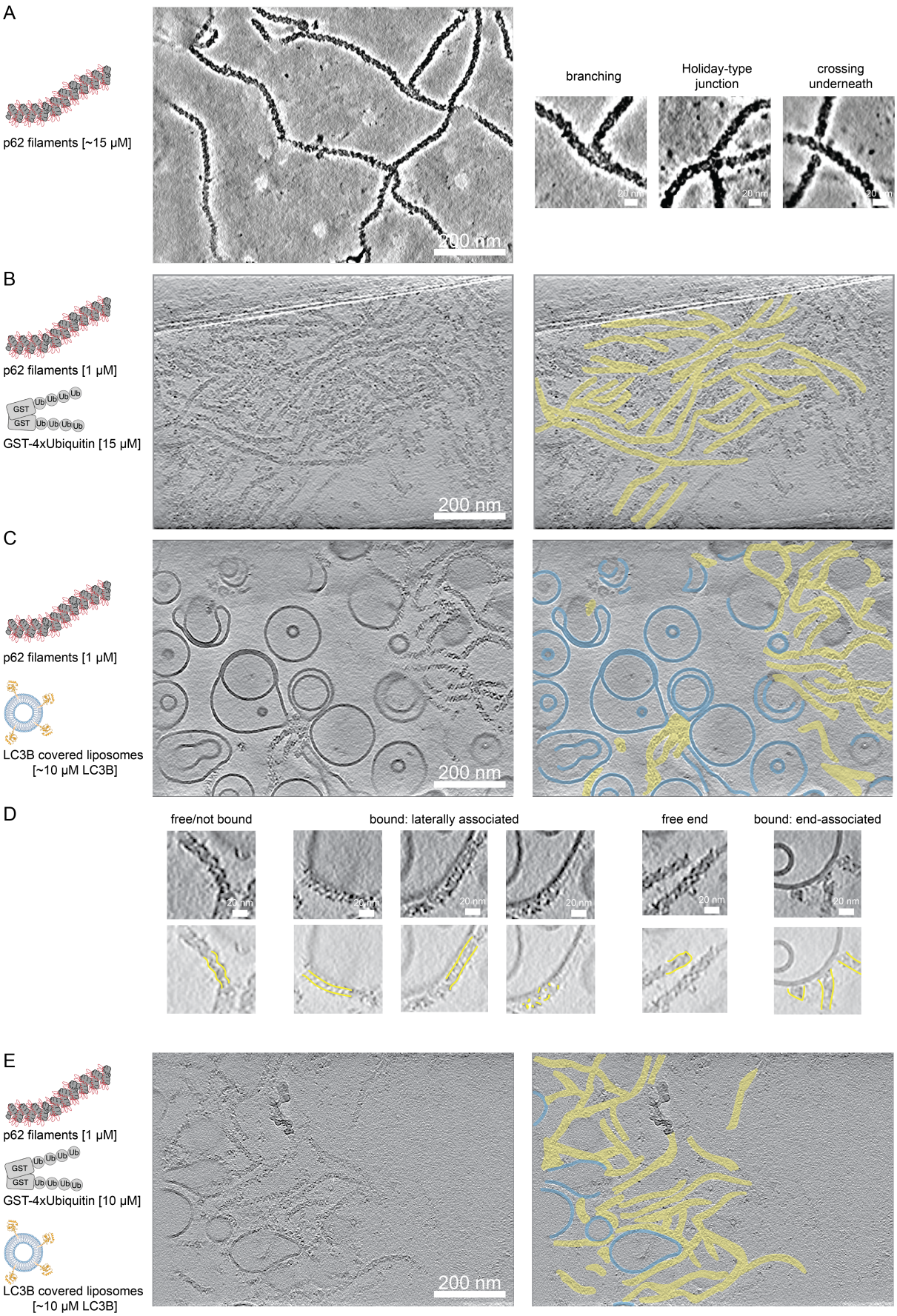
A
p62 filaments [~15 µM]
200 nm
branching
Holiday-type junction
crossing underneath
20 nm
B
p62 filaments [1 µM]
GST
Ub
GST-4xUbiquitin [15 µM]
200 nm
C
p62 filaments [1 µM]
LC3B covered liposomes [~10 µM LC3B]
200 nm
D
free/not bound
bound: laterally associated
free end
bound: end-associated
20 nm
E
p62 filaments [1 µM]
GST-4xUbiquitin [10 µM]
LC3B covered liposomes [~10 µM LC3B]
200 nm

292

Figure 3: p62 filament interactions with LC3b-conjugated liposomes and poly-ubiquitin visualized by cryo-electron tomography. (A) Left. Representative micrograph of p62 filaments recorded with Volta phase plate. Gold fiducials were computationally removed in the locations of the smooth circles. Right. Close-up insets showing the regular 14 nm pitch features along the filament. p62 filament were found crossing each other underneath (left), branching by 90° (center) and cross overs as in the Holliday junctions of DNA (right). (B) Left. Upon addition of GST-4xUbiquitin, the formation of parallel p62 filament bundles was observed. Right. Segmentations of closely packed p62 filaments aligned in parallel. (C) The addition of pre-formed p62 filaments to LC3b-conjugated small unilamellar vesicles (SUVs) showed bound and unbound p62 filaments. (D) Top. p62 filaments were found not-bound (left), bound laterally associated with the membrane (left center), free ends (right center) or through their ends (right). Bottom. Outline of p62 densities is highlighted in yellow. For laterally associated p62, regular helical and unwound assemblies were observed. (E) Co-incubation of GST-4xUbiquitin and LC3b-conjugated SUVs led to a dense network of p62 bundled filaments partially bound to SUVs.

ATG5 knockdown accumulates co-localized p62 punctae and lipid droplets

In order to further our understanding on the structural organization of autophagy receptor p62, we decided to visualize the cargo receptor in cells. Capturing rare and transient p62 punctae is challenging, therefore, we turned to a model system of ATG5 depletion that was shown to increase the size and number of p62 punctae in MEF cells and mice (Morishita et al., 2013; Pankiv et al., 2007) along with increased numbers of lipid droplets (Singh et al., 2009). We stalled autophagy by treating human RPE1 cells stably expressing mCherry-p62 with siRNA against ATG5 for 72 hours. To validate the phenotype upon ATG5 knockdown, we detected p62 punctae as well as lipid droplets by confocal fluorescence microscopy using mCherry-p62 and the lipid-droplet specific Lipi-Blue dye, respectively, in conditions of no transfection, mock transfection and transfection with ATG5 siRNA (**Figure 4A-C**). As a control for mCherry-p62, we imaged lipid droplets in RPE1 reference cells with Lipi-Blue after no transfection, mock transfection and transfection with ATG5 siRNA using confocal microscopy (**Figure 4D-F**). In order to confirm successful ATG5 siRNA knockdown, we performed a Western blot of the RPE1 cells showing a reduction in ATG5 expression levels by 90 % in comparison with the control samples (**Figure 4G**). When incubated with ATG5 siRNA, the number of p62 punctae was highest at an average of 37 per mCherry-p62 RPE1 cell (**Figure 4H**). In the presence of ATG5 siRNA, the average size of the lipid droplets increased from 0.30 to about 0.45 μm^2 for mCherry-p62 RPE1 and for RPE1 cells (**Figure 4I**), while we also counted the highest number of co-localized p62 punctae in comparison with no or mock siRNA (**Figure 4J**). Interestingly, in our mock transfected cells we already observed a moderate increase in lipid droplet sizes and p62 punctae possibly due to the fact that cationic lipid mixtures have been observed to induce

335 autophagy promoting LC3 conversion and p62 degradation (Man et al., 2010; Mo et
336 al., 2012). Together with the autophagy-stalling effect of ATG5 siRNA, they likely
337 contribute to further enrichment of p62 positive structures. In conclusion, when
338 transfecting RPE1 cells with ATG5 siRNA, we observed an accumulation for p62
339 punctae and lipid droplets as well as a size increase for lipid droplets. The
340 characterized condition of ATG5 knockdown may be well suited for the in situ
341 visualization of p62 punctae as p62 cargo uptake in the lysosome is impaired.

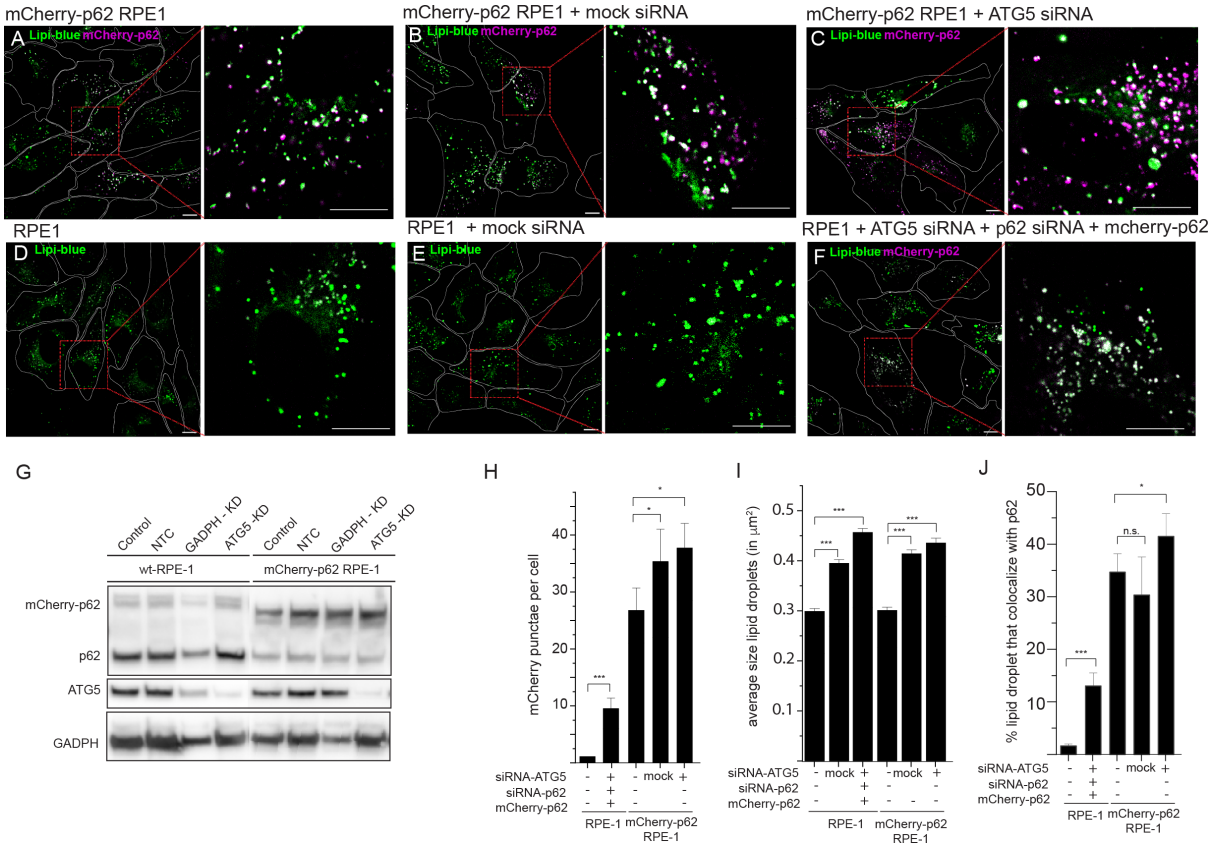

342

343 **Figure 4: Confocal fluorescence microscopy of p62 punctae and lipid droplets upon**
344 **ATG5 knockdown. mCherry-p62 RPE1 cells stained with Lipi-Blue for 24 hours at**
345 **conditions of (A) no transfection, (B) 72 hrs after a mock transfection with RNAiMax**
346 **and (C) 72 hrs after a transfection with ATG5 siRNA. Reference RPE1 cells stained**
347 **with Lipi-Blue for 24 hours at conditions of (D) no transfection, (E) 72 hrs after a**
348 **mock transfection with RNAiMax and (F) 72 hrs after a transfection with ATG5**
349 **siRNA. (G) Western blot confirming the knockdown of ATG5 expression including**
350 **a control knockdown of GADPH. Quantifications for the displayed samples: (H)**
351 **Number of p62 structures per cell, (I) size of lipid droplets and (J) number of p62**
352 **punctae and lipid droplets colocalizations. Statistical significance was determined**
353 **with a t-test: *=p<0.1, =p<0.01,* =p<0.001**

354 p62 encapsulates lipid droplets by a discontinuous coat of variable
355 thickness

356 Based on the established condition of accumulated colocalized p62 punctae and lipid
357 droplets, we set out to perform detailed in situ structural analyses to study p62 during

358 lipid droplet cargo recognition. The RPE1 cells were grown under the same conditions
359 described above and placed on micropatterned electron microscopy grids, vitrified,
360 subsequently thinned to ~150 nm using a focused ion beam (FIB) and visualized using
361 a scanning electron microscope (SEM) (**Figure 5A**). To verify that the lamella
362 contained mCherry-p62, we imaged the sample using an integrated cryo-fluorescence
363 microscope and correlated it with the FIB-SEM image (Smeets et al., 2021) (**Figure**
364 **5B**). When we visualized these p62 structures using super-resolution cryo-confocal
365 microscopy, they showed circularly resolved mCherry-p62 signal on their rim
366 suggesting the cargo encapsulation by the autophagy receptor p62 (**Figure 5C**). At
367 these sites, a total of 25 tomograms were recorded while those with green
368 autofluorescence from lysosomes were not further analyzed. In the reconstructed
369 tomograms, we identified characteristic structures made of a homogeneous texture of
370 spherical shape suggestive of a lipid droplet (Ganeva et al., 2023) (**Figure 5D**) in
371 agreement with the frequent co-localization of p62 and lipid droplet punctae
372 demonstrated above. A dark and highly dense layer was found surrounding the droplet
373 in addition to a single phospholipid bilayer. The homogeneously textured spheres were
374 similar in size measuring between 510 - 530 nm (**Figure 5E**). The surrounding layer,
375 or coat, varied in thickness within a single structure as well as between structures
376 ranging between 4 and 27 nm, with a mean of 12.6 nm (**Figure 5F** and
377 **Supplementary Figure 4**). The distance between the surface of the sphere and the
378 surrounding single lipid membrane was relatively uniform at 13.8 nm with some
379 weaker protein densities filling this space while other densities connecting these two
380 structures (**Figure 5G/H**). The segmented tomograms revealed that when the layer
381 was thin, patches or islands of dark contrast were found distributed around the surface
382 of the lipid droplet (**Supplementary Figure 5**). However, when the layer was thick, it
383 was completely continuous. Next to the lipid droplet, several small vesicles between
384 35 and 52 nm in diameter were observed consistent with previously described ATG9A
385 vesicles (Mailler et al., 2021). In summary, ATG5 knockdown in human RPE1 cells
386 yielded p62 positive spherical structures of 500 nm diameter composed of an inner
387 lipid droplet and a p62-containing, dense layer of variable thicknesses covering the
388 surface surrounded by a single bilayer membrane.

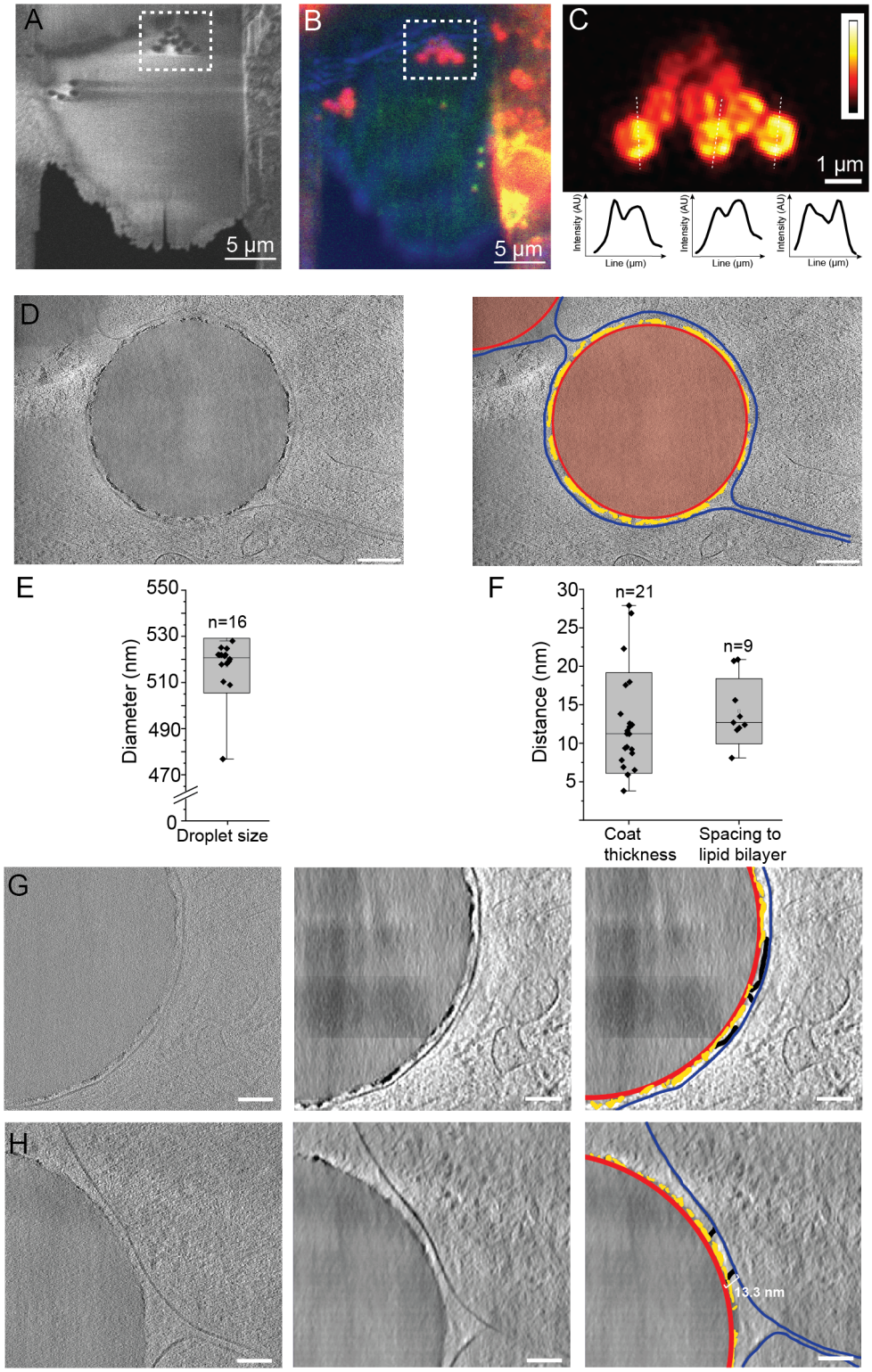

Figure 5: Ultrastructural in situ characterization of p62-encapsulated lipid droplets. (A) Scanning electron microscopy image of a lamella generated from an EM grid grown with RPE1 cells. (B) Correlated fluorescence image of the corresponding lamella recorded with a reflected light channel and fluorescent channels of 595 nm for mCherry-p62 and 515 nm for autofluorescence. (C) Super-resolution cryo-confocal fluorescence image recorded at 561 nm for mCherry-p62 showed three p62-positive structures resolving a circular fluorescence signal as displayed in three corresponding intensity profiles below. (D) Tomographic gray-scale z-slice

398 **through the homogeneous density sphere surrounded by a dark high-contrast layer**
399 **with an enwrapped single membrane. Scale bar 100 nm. (E) Segmented and labeled**
400 **structure superimposed on gray-scale z-slice, light red: lipid droplet with red:**
401 **droplet surface, yellow: dark and high-contrast surrounding p62 layer and blue:**
402 **single lipid membrane. (F) Left. Box plot indicates a well-defined lipid droplet**
403 **diameter of about 520 nm. Right. Box plot of measured distances of observed dark**
404 **layer thickness and spacing of droplet surface to enwrapped single lipid bilayer.**
405 **(G) Tomographic z-slice of half a lipid droplet in raw grayscale (left), denoised**
406 **grayscale (center) and superimposed labeled structures of droplet surface (red),**
407 **dark layer (yellow), weaker protein density (black) and enwrapping single lipid**
408 **bilayer (blue). Scale bar 50 nm. (H) Tomographic z-slice of another droplet showing**
409 **the spacing of 13.3 nm between droplet surface and single lipid bilayer. Scale bar**
410 **50 nm.**

411 Elemental analysis reveals calcium and phosphorus in the p62 positive 412 layer

413 Given the strong observed intensity of the surrounding p62-positive layer with respect
414 to the grey levels of the lipid droplet and cytosol, we wondered whether non-organic
415 elements contributed to the high contrast. To address this question, we employed
416 scanning transmission electron microscopy (STEM) coupled with energy-dispersive X-
417 ray (EDX) spectroscopy to record element-specific X-rays from the mCherry-p62
418 RPE1 lamella treated with ATG5 siRNA investigated above (**Figure 6A-D**). For this
419 sample, we acquired STEM images on a high-angle annular dark-field (HAADF)
420 detector and simultaneously recorded the back-scattered EDX signal (**Figure 6E**). The
421 EDX signal was averaged over the excised regions of the cytosol, lipid droplet core
422 and the p62 coat (**Supplementary Figure 6**). For the cytosol, we detected mostly
423 carbon (C), nitrogen (N) with low and oxygen (O) with high intensity at approx. 300,
424 400 and 500 eV, respectively. For the lipid droplet, we observed enriched C in
425 comparison with the cytosol, reduced N and O consistent with the presence of triacyl
426 glycerides and sterols within the sphere of lipid droplets. In both regions, no inorganic
427 elements were observed at higher energies. For the p62 coat, we found the C, N, O
428 signal comparable to the cytosol with clear additional inorganic signals of magnesium
429 (Mg), calcium (Ca) and phosphorus (P) at 1250, 2000 and 3800 eV, respectively,
430 supporting the observation of the relatively strong contrast in the raw tomograms. The
431 detected high levels of Ca and P suggest the presence of calcium phosphate. As a
432 control, we focussed on lipid droplets showing no p62 colocalization and obtained a
433 very similar EDX signal (**Supplementary Figure 7**). Other p62 positive single-
434 membrane vesicular structures resembling lysosomes showed no differences in EDX
435 profiles between the vesicular area and the cytosol (**Supplementary Figure 8**).

436 Given the unexpected finding of inorganic elements located in the p62 coat, we tested
437 whether the addition of Ca^{2+} ions had an effect on purified p62 filaments. When

438 increasing the $CaCl_2$ concentrations from 100 nM to 100 mM, we observed a bundling
439 of p62 filaments at 100 mM $CaCl_2$ in negative staining EM (**Figure 6F-H**). Moreover,
440 when testing other divalent cations such as Zn^{2+} and Mg^{2+}, we found that the addition
441 of $ZnCl_2$ had a stronger clustering effect already visible at 100 μM, while the addition
442 of $MgCl_2$ did not show a significant bundling (**Supplementary Figure 8**). Together,
443 these experiments show that the observed p62-positive structures correspond to lipid
444 droplets surrounded by a coat made of p62, including significant amounts of calcium
445 (**Figure 6I**) that also promotes the formation of p62 oligomer bundles in vitro and may
446 explain the characteristic dense layer observed in the tomograms.

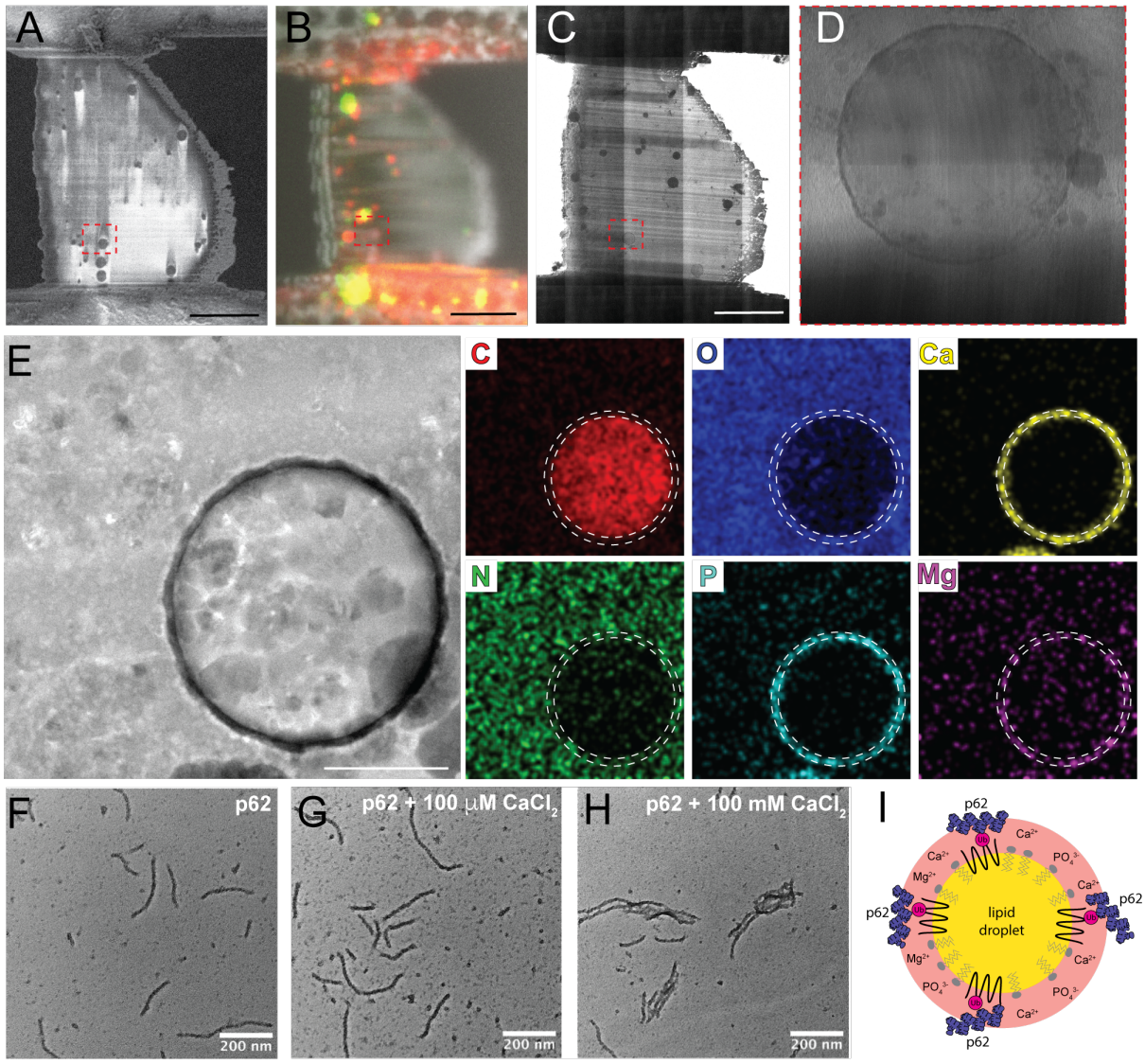

447

448 **Figure 6: Compositional elemental analysis of p62-encapsulated lipid droplets**
449 **using energy dispersive X-ray (EDX) spectroscopy. (A) Scanning electron**
450 **microscopy (SEM) image of milled lamella with inset of characterized lipid droplet.**
451 **(B) Correlated SEM image superimposed with a reflected light channel and**
452 **fluorescent channels of 595 nm for mCherry-p62 and 515 nm for autofluorescence.**
453 **(C) Transmission electron microscopy image of corresponding lamella. (D)**
454 **Enlarged image of p62-positive lipid droplet. (E) High-angle annular dark-field**

455 **scanning transmission electron microscopy (HAADF-STEM) image of droplet of**
456 **interest with corresponding EDX signals for Carbon in red (C), Oxygen in blue (O),**
457 **Calcium in yellow (Ca), Nitrogen in green (N), Phosphorus in cyan (P) and**
458 **Magnesium in purple (Mg). Scale bar 500 nm. Negative stain EM images of (F)**
459 **purified p62 filaments, (G) with 100 μM $CaCl_2$ and (H) 100 mM $CaCl_2$. (I) Model**
460 **summary of analyzed p62 droplet structures: the lipid droplet devoid of any**
461 **phospholipids is encapsulated by p62-positive layer that is rich in $CaPO_4$.**

462 Discussion

463 In the current study, we addressed the structural organization of the archetypical
464 autophagy receptor p62/SQSMT1 at various levels of resolution. Initially, we
465 determined the cryo-EM structure of full-length p62 at 4.5 Å global resolution revealing
466 the double helical filament PB1 scaffold with peripheral lower-resolution densities
467 corresponding to the ZZ-domain and C-terminal part (**Figure 1**). Interestingly, the
468 addition of LC3b led to a shortening of the filament at higher concentrations while GST-
469 4xUb resulted in the bundling of filaments to phase-separated entities consistent with
470 solvent-exposed accessible binding sites to LC3b and ubiquitin through the major
471 groove of the filament (**Figure 2**). When p62 filaments were bound to LC3b-conjugated
472 SUVs, we observed a lateral association on model membranes of the p62 filament
473 while maintaining regular p62 oligomer arrays (**Figure 3**). Moreover, we visualized p62
474 structures in cells using fluorescence light microscopy, correlative light and electron
475 microscopy (CLEM) followed by cryo-ET in a p62-enriched phenotype due to ATG5
476 knockdown (**Figure 4 and 5**). The detailed ultrastructural analysis of this autophagy-
477 stalled phenotype revealed a high-contrast layer of p62-positive structures
478 surrounding lipid droplets due its enriched calcium phosphate content (**Figure 6**).

479 In contrast to the previously determined PB1 assemblies (Jakobi et al., 2020), the here
480 determined full-length p62 filament structure formed a double-helical filament
481 architecture widely known from the classical DNA double helix model (Watson & Crick,
482 1953). The full-length structure revealed two well-resolved antiparallel PB1 scaffold
483 strands while the PB1 domain-only assemblies have one or two additional PB1 strands
484 inserted into the helical assembly leading to an almost closed tube. In the full-length
485 structure, the space required by the additional 340 C-terminal amino acids restricts the
486 assembly to two antiparallel PB1 strands leaving space for a major groove. Our binding
487 assays showed a shortening the filament upon LC3b interaction in agreement with
488 model predictions of the LIR motif to be accessible in solution through the major
489 groove. In our solution studies, we also found the p62 concentrations to be critical for
490 detecting clear binding effects such as shortening or filament bundling in the case of
491 4xGST-Ub. In addition, we also observed bundling of p62 filaments upon addition of
492 divalent cations in $CaCl_2$ and $ZnCl_2$ solutions (see **Figure 6G-H**). Multivalency

493 available in a polymer and across polymers may mediate the bundling, e.g., when
494 several UBA domains from different filaments bind to polyubiquitin or when parts of
495 ZZ-domains originating from multiple p62 filaments share the coordination of divalent
496 cations such as Zn^{2+} and Ca^{2+}. Multivalent interactions mediated by GST4xUb have
497 been shown to promote phase separation of p62 (Zaffagnini et al., 2018a). In the cell,
498 we expect some of these interactions to be present on membrane surfaces through
499 membrane-linked p62 polymers and oligomers, which provides the principal benefit of
500 high local concentrations offered for low-affinity interactions to be enhanced by high
501 avidity binding. In support of this concept, when we linked the binding partner LC3b
502 (Pankiv et al., 2007) to the liposome membrane surface, upon p62 filament addition
503 we did not observe a complete filament disassembly, rather we observed a lateral
504 binding of the filament. In the images at physiological pH, we also found an unwinding
505 and structural opening up of the double-helical filament architecture located on the
506 membrane surface. In such an assembly configuration, previously inaccessible
507 available binding sites in the interior will become accessible in an opened p62 “bubble”
508 structure while still maintaining functional polymers and oligomers. The unwinding,
509 structural opening and re-arrangement of the filament architecture on membrane
510 surfaces may provide a higher level of regulating access of binding partners to the
511 multiple binding sites in p62.

512 After the in vitro structural and biochemical work, we turned to the RPE1 cellular model
513 to investigate the ultrastructural details of p62 using cryo-ET. In order to enrich p62
514 structures, we depleted ATG5 that is an essential member of the core machinery
515 driving autophagy progression (Mizushima et al., 2001; Morishita et al., 2013; Pankiv
516 et al., 2007). During autophagy, ATG5 is covalently linked to ATG12 that together with
517 ATG16L is required for LC3-I conjugation to the membrane in the form of LC3-II and
518 thereby accomplishing phagophore expansion (Otomo et al., 2013). Upon ATG5
519 depletion, characteristic LC3 punctae and autolysosomes cannot form leading to an
520 accumulation of cargo, e.g., when lipid droplet breakdown is inhibited, triacylglycerides
521 have been shown to accumulate (Singh et al., 2009). Moreover, in mice, ATG5
522 knockouts have severe consequences for neuronal development leading to delays in
523 maturation as ATG5 appears to be essential for the survival of adult-generated
524 neurons (Xi et al., 2016). Based on the near-native visualization using in situ cryo-
525 CLEM in RPE1 cells, we observed p62-positive structures wrapping around lipid
526 droplets made of triacylglycerides giving rise to homogeneous density in the electron
527 tomograms and characteristic EDX signals. Lipid droplets have been observed in the
528 diameter ranges of 100 nm to over 1 µm in size (Schott et al., 2019) while the here

529 observed ones had relatively narrow distribution of 500 to 540 nm. Lipophagy has
530 been described as being initiated by the ubiquitination of PLIN proteins embedded in
531 the phospholipid monolayer surrounding the lipid droplets (Tsai et al., 2017).
532 Moreover, LC3 and p62 were also described as forming punctae on the surface of lipid
533 droplets (Robichaud et al., 2021). In this way, they are thought to induce the formation
534 of the autophagosomal membrane surrounding the lipid droplets. While in ATG5
535 depleted cells LC3-II is not present on the membrane, p62 has been shown to still be
536 capable of recruiting cargo, ATG9A vesicles, ATG16L vesicles and FIP200
537 condensates (X. Feng et al., 2023; Itakura & Mizushima, 2011). Possibly, the small
538 vesicular structures we observed next to the p62 positive lipid droplets (see
539 **Supplementary Figure 5B**) may correspond to previously observed ATG9 vesicles
540 (30-60 nm) or ATG16L vesicles (Dupont et al., 2014; Mailler et al., 2021; Puri et al.,
541 2013; Yamamoto et al., 2012).

542 When we segmented tomography data of the ATG5 depleted cells, we observed p62
543 coating of various thicknesses on the lipid droplets. In close vicinity, we often found a
544 single, unclosed membrane (see **Supplementary Figure 5A**) enwrapping the coated
545 lipid droplet. In the ATG5 knockdown condition, we do not expect a bona fide
546 autophagy double membrane to be present. Due to the observed connections to
547 membrane stacks, it appears plausible that we visualized recruited ER membrane
548 unable to extend and seal off the lipid droplets due to the lack of lipidated LC3-II. In
549 our p62-positive structures, we also observed 13.3 nm wide protein density connecting
550 the droplet surface/coat and the enwrapped membrane in addition to elongated flexible
551 density. The density is not compatible with regular helical p62 filaments used for
552 structure determination above as no pitch repeat distance along the long axis is
553 discernible. Alternative assemblies, however, such as unwound or opened p62
554 filaments share similar width dimensions to the measured 13.3 nm. Other potential
555 molecules of the autophagy core machinery include ATG2A/B (Y. Wang et al., 2024),
556 the ULK1 complex (Chen et al., 2023) or FIP200 (Chen et al., 2023) all of which have
557 elongated shapes but are either longer or shorter than the observed densities. Clearly,
558 more research and improved imaging features will be required to confirm the identity
559 of the protein complexes involved in the studied p62-positives structures.

560 The p62-lipid droplet structures we have visualized in this study were found
561 surrounded by dark layers. We identified them to be mainly composed of calcium,
562 phosphorus and magnesium using EDX spectroscopy suggesting high levels of
563 calcium phosphate. Previously, the same approach has been used on vitreous
564 sections and other frozen hydrated samples (Kumar et al., 2020; WOLF et al., 2015;

565 Wolf et al., 2017; Zierold et al., 1984) while in this study we employed it on FIB-milled
566 lamella. A dark high-contrast layer had been observed before in close proximity to lipid
567 droplets in the context of autophagy using plastic section electron microscopy
568 (Robichaud et al., 2021; Schott et al., 2019; Singh et al., 2009). We do not claim that
569 the previously imaged structures correspond to structures we observed, nevertheless
570 the resemblance is noteworthy. For some time, intracellular calcium levels have been
571 linked to autophagy as rapamycin-induced autophagy led to an increase in cytosolic
572 Ca^{2+} concentration and a decrease in the calcium ER leak rate both of which were
573 independent of LC3 lipidation (Decuypere et al., 2013). Moreover, the addition of a
574 calcium chelator such as BAPTA-AM was shown to be sufficient to block autophagy
575 initiation (MacVicar et al., 2015). In a more recent study, evidence was provided that
576 brief calcium transients are released from the ER, which trigger FIP200 punctae
577 formation and modulate phase separation at the autophagosome assembly site (Q.
578 Zheng et al., 2022). In yeast, calcium has also been shown to be required for
579 autophagy initiation under glucose starvation conditions (Yao et al., 2024). It seems
580 plausible that in this study we directly observed calcium ions bound to the lipid droplet
581 surface originally released from the ER, which help to organize the early stages of
582 lipophagy. Given the demonstrated bundling capabilities of p62 by divalent cations in
583 solution, it is possible that the observed dark p62-positive coat found on the cargo lipid
584 droplet is the result of calcium transients release from the ER that orchestrate the early
585 stages of autophagy machinery recruitment. Further research will be required to fully
586 establish the links between the here presented cryo-EM structure, biochemical binding
587 properties, higher-order organization, in situ ultrastructure and autophagy initiation.

588

Supplementary Figures

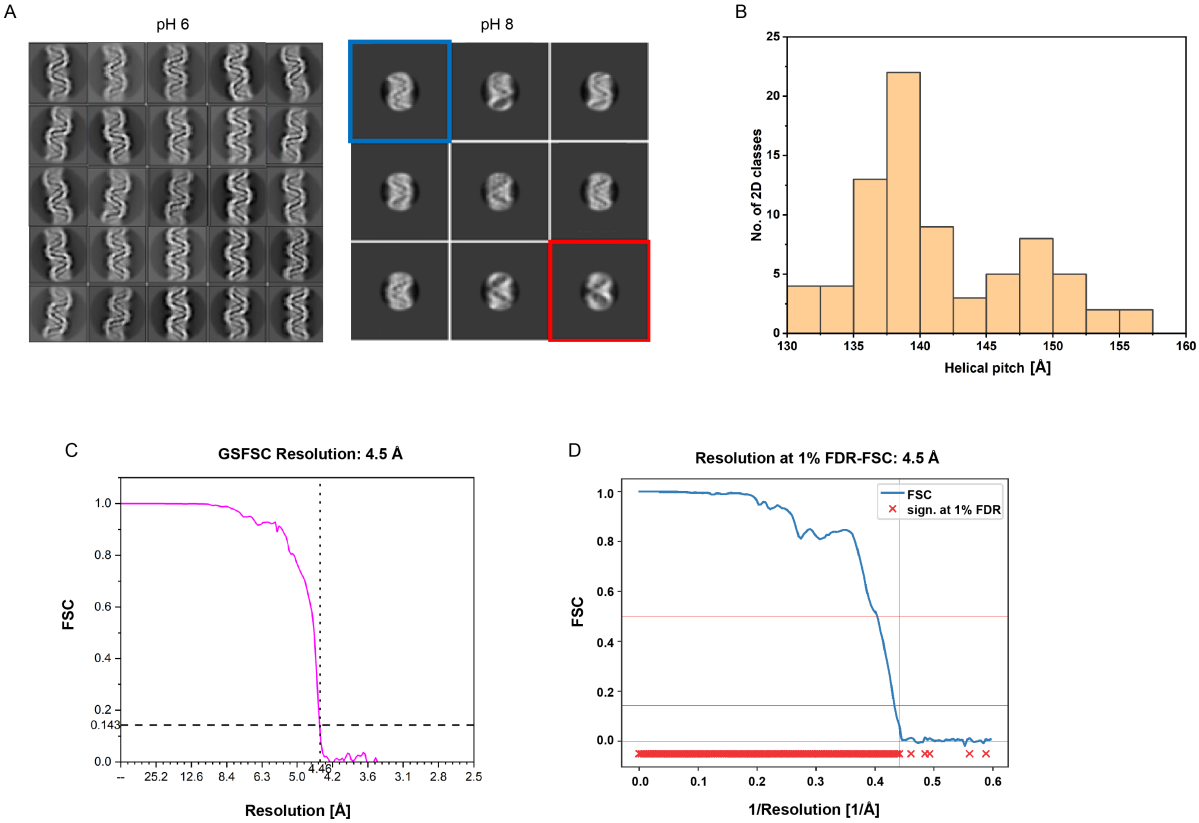

Supplementary Figure 1: p62 filament sample optimization, helical pitch of p62 filaments and resolution assessment of p62 cryo-EM structure. (A) 2D classification at pH 6 (left) and pH 8 (right). At pH 6, the classes show a regular helical architecture. At pH 8 almost 60% of the particles show an unwinding of the two strands (red), whereas 40% of the particles still show a closed form of the filament (blue). (B) Helical pitch distribution of p62 filaments ranges from 130 to 160 Å. (C) Fourier shell correlation (FSC) curve of the p62 filament density map indicates a resolution according to the cutoff FSC(0.143)=4.5 Å. (D) FDR-FSC curve indicates a resolution of 4.5 Å.

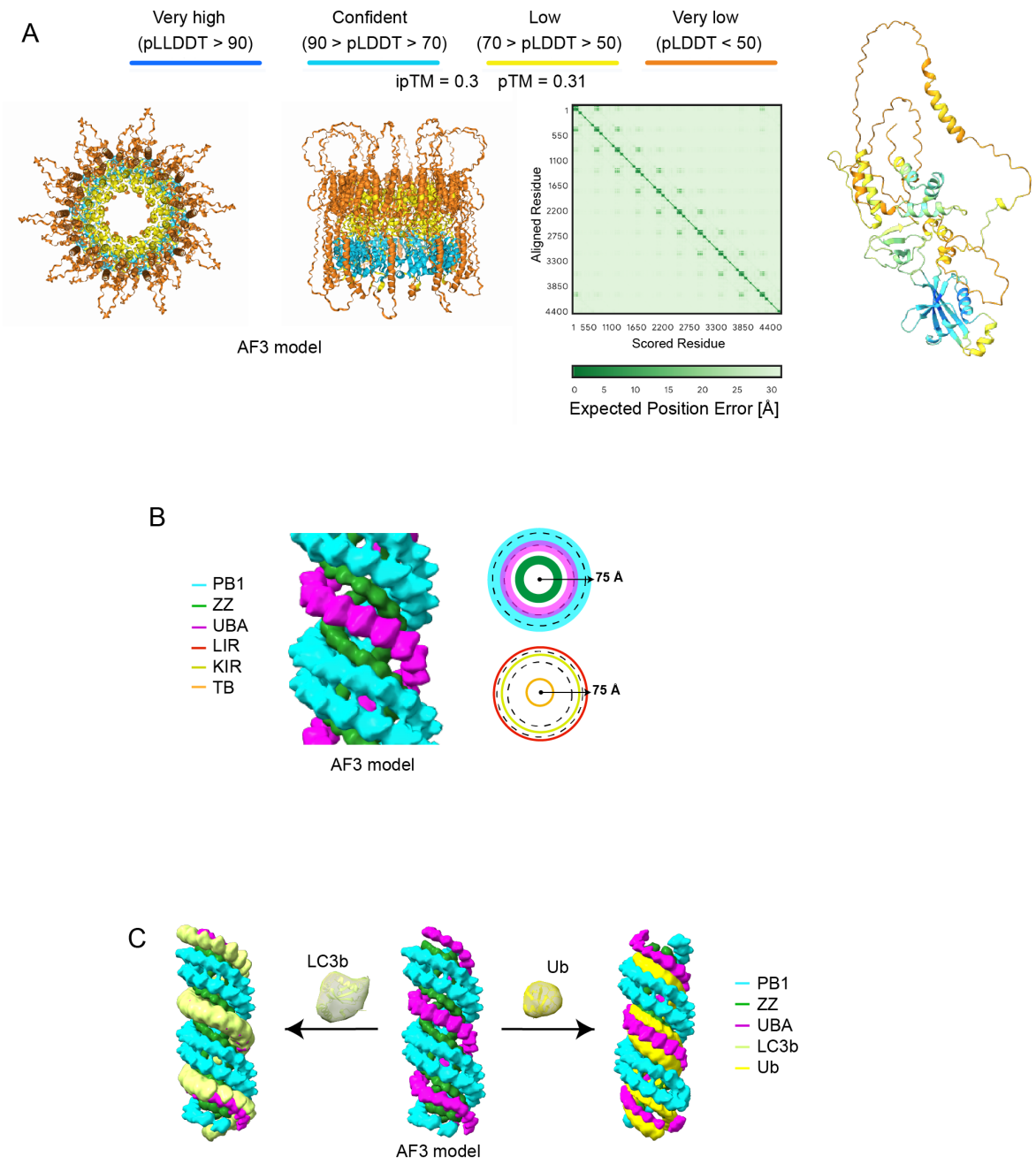

Supplementary Figure 2: AlphaFold3 prediction of p62 assembly, domain localization, binding of LC3b and competition with ubiquitin. (A) Left. AlphaFold3 (AF3) model of the p62 decamer ring (top and side view), colored according to a per-atom confidence estimate. Predicted aligned error (PAE) plot reveals spatial proximity of the domains. Right. Single p62 molecule AF3 prediction excised from 10-mer colored with per-residue model confidence estimate. (B) p62 filament model of AF3 predictions showing PB1 (cyan), ZZ (green) and UBA (magenta) domains rendered at 15 Å resolution. Top views showing relative position of subunits and binding sites and their radial distance from the center of the filament. The two dotted lines mark the

position of the PB1 domain that corresponds to the strongest observed density in the cryo-EM map. (C) p62 filament models of AF3 predictions rendered at 15 Å resolution with LC3b (left) or ubiquitin (right) bound.

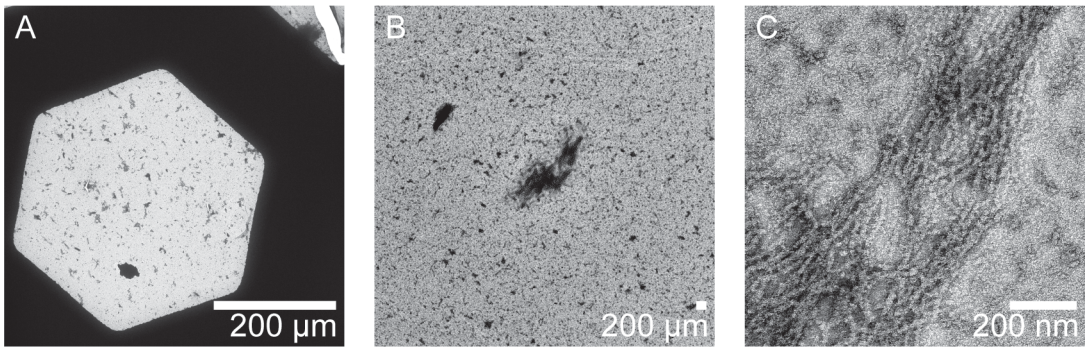

Supplementary Figure 3: Phase separation of p62 filaments induced by addition of GST-4xUbiquitin. p62 filaments at 1 μM concentration were mixed with 15 μM GST-4xUbiquitin, incubated for four minutes and subsequently negatively stained. The resulting phase separation droplets were imaged at (A) 100x, (B) 8,500x and (C) 57,000x magnification revealing dense clusters of p62 filament bundles.

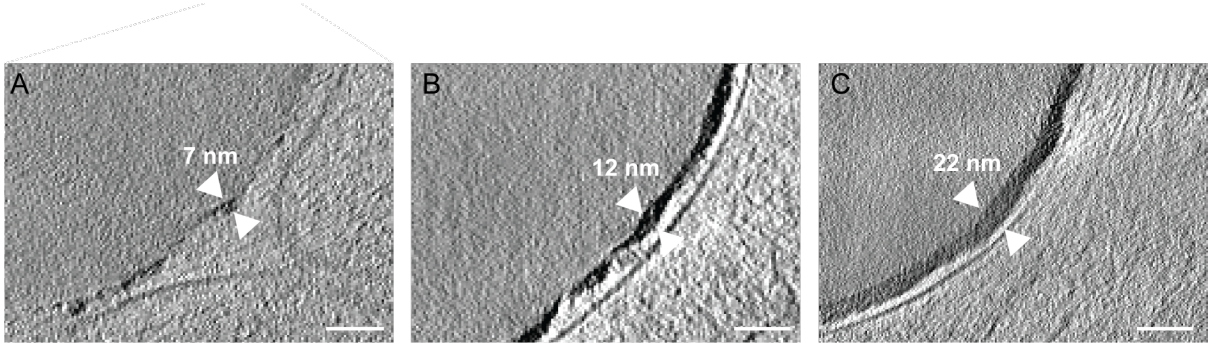

Supplementary Figure 4: Different thicknesses of droplet coats. Lipid droplets are coated by a high-contrast layer of different thicknesses measuring (A) 7 nm, (B) 12 nm and (C) 22 nm. Scale bar 50 nm.

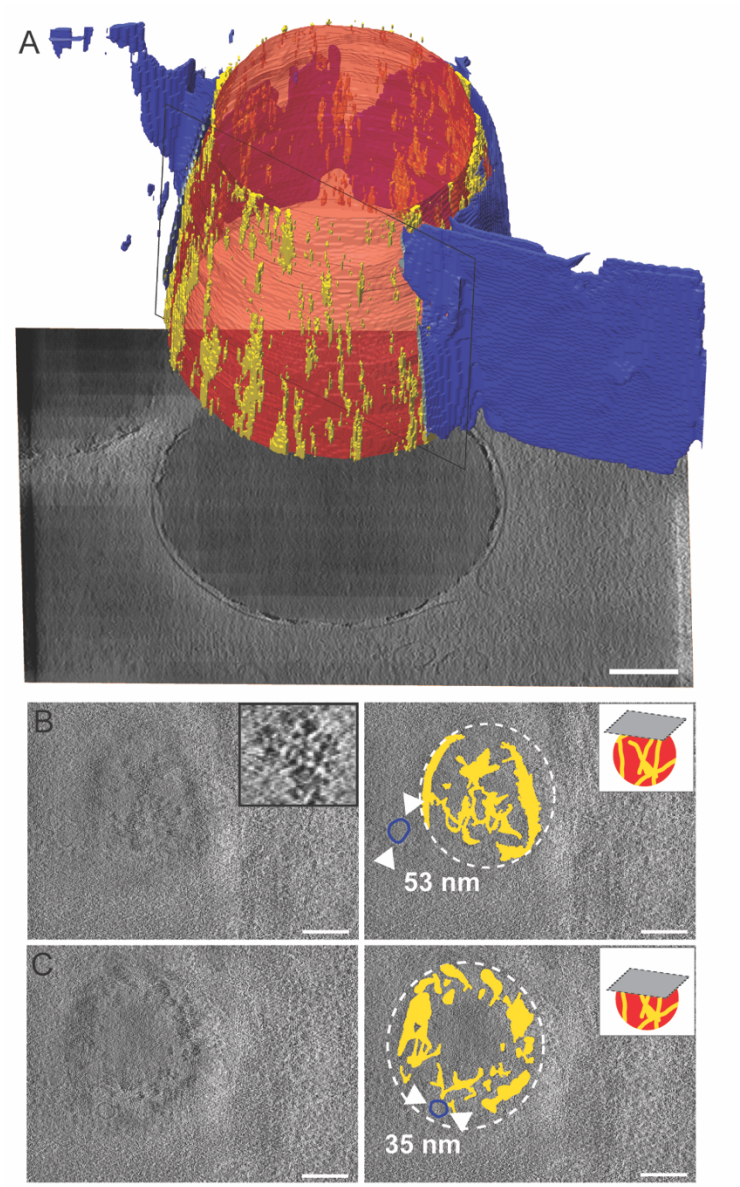

Supplementary Figure 5: Segmented tomogram showing a thin discontinuous high-contrast p62-positive coat surrounding the lipid droplet. (A) Segmented tomogram rendered in three dimensions: lipid droplet (red), p62-positive coat (yellow) enwrapped by a single lipid bilayer stack (blue). The membrane was opened up using a clipping plane (black rectangle) for easier visualization. (B) Upper z-section through segmented tomogram reveals the thin discontinuous surface coating around the lipid droplet. Inset shows the granular nature of the surface coating. (C) Center z-section of the same lipid droplet. Small vesicular structures (blue) of 35 and 53 nm diameter are also visible in both z-slices. Scale bar 100 nm.

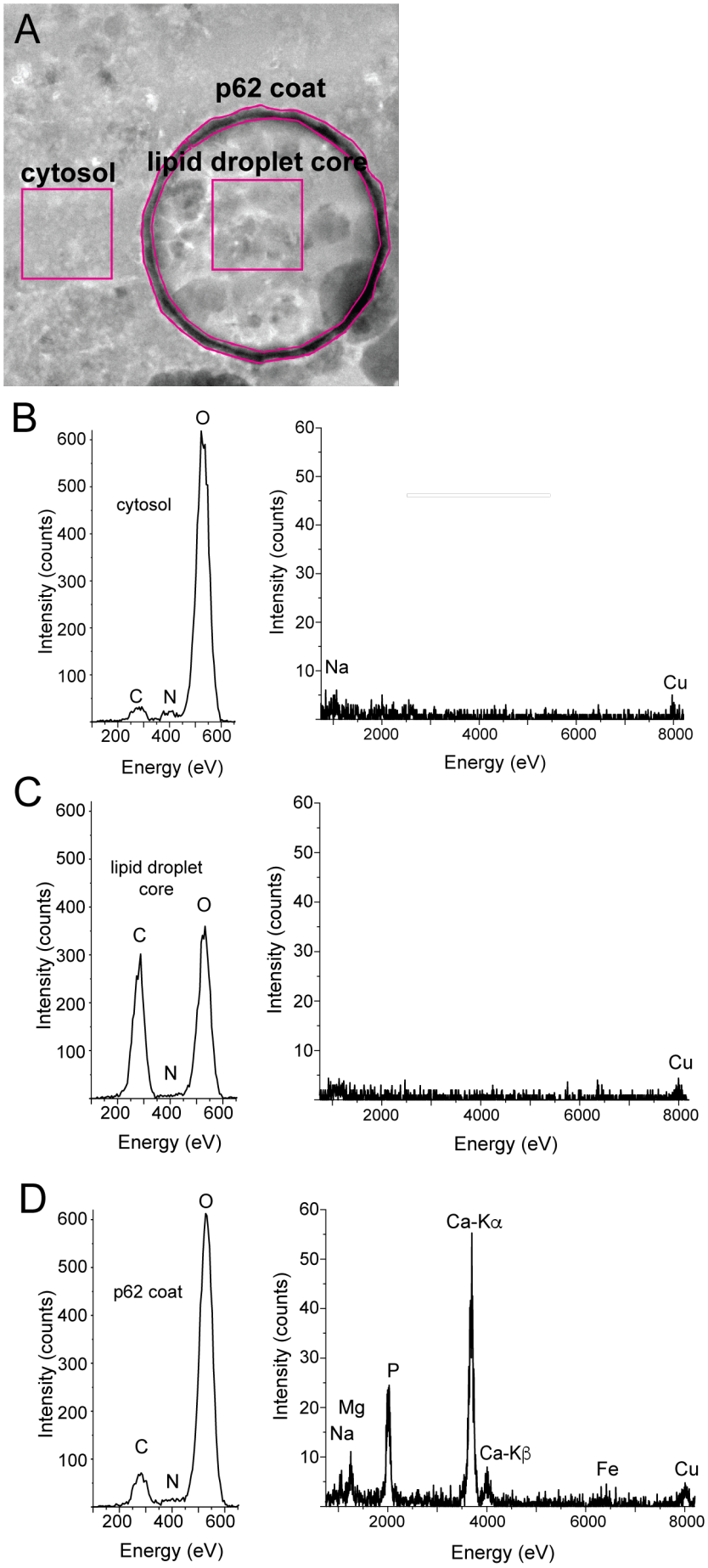
A
p62 coat
cytosol
lipid droplet core
B
cytosol
O
C
N
Intensity (counts)
Energy (eV)
Na
Cu
C
lipid droplet
core
O
C
N
Cu
D
p62 coat
O
C
N
Ca-Kα
P
Mg
Na
Ca-Kβ
Fe
Cu

633

634 **Supplementary Figure 6: Energy-dispersive X-ray (EDX) spectroscopy**
635 **combined with STEM imaging of p62-positive lipid droplets.** (A) HAADF-STEM
636 image of p62 positive lipid droplets. Insets indicate the regions used for summing of
637 EDX signals. The same number of pixels were summed in all regions. X-ray spectra
638 showing which elements are present in the different areas; in (B) cytosol, (C) lipid
639 droplet core and (D) dense p62 positive coat, respectively. Peaks were marked with
640 their respective elements. The weak copper (Cu) peak originates from the copper
641 sample holder used.

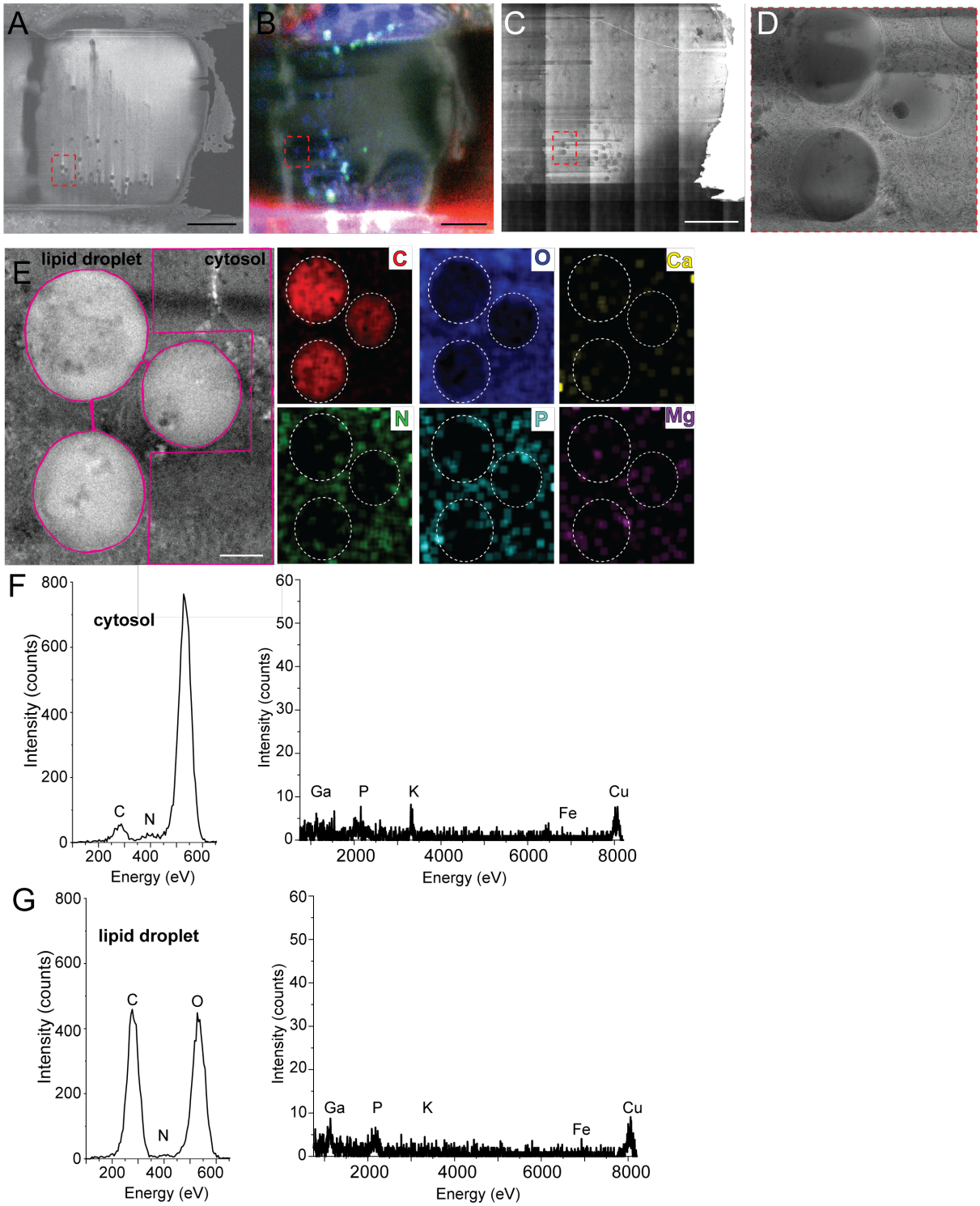

Supplementary Figure 7: Energy-dispersive X-ray spectroscopy (EDX) combined with STEM imaging of native lipid droplets. (A) Scanning electron microscopy images of lamella with visible droplets in inset. Scale bar 5 μm. (B) SEM image superimposed with fluorescent image of Lipi-Blue dye. (C) Overview image of corresponding recorded transmission electron microscope (TEM). (D) Three spatially close lipid droplets in higher magnification TEM image. (E) HAADF-STEM image of three adjacent lipid droplets corresponding elemental images of carbon (C), oxygen

650 (O), calcium (Ca), nitrogen (N), phosphorus (P) and magnesium (Mg). The image
651 shows two insets of the cytosol and droplet region used for subsequent averaging.
652 EDX spectra of (F) cytosol region and (G) lipid droplet regions. Scale bar 200 nm.

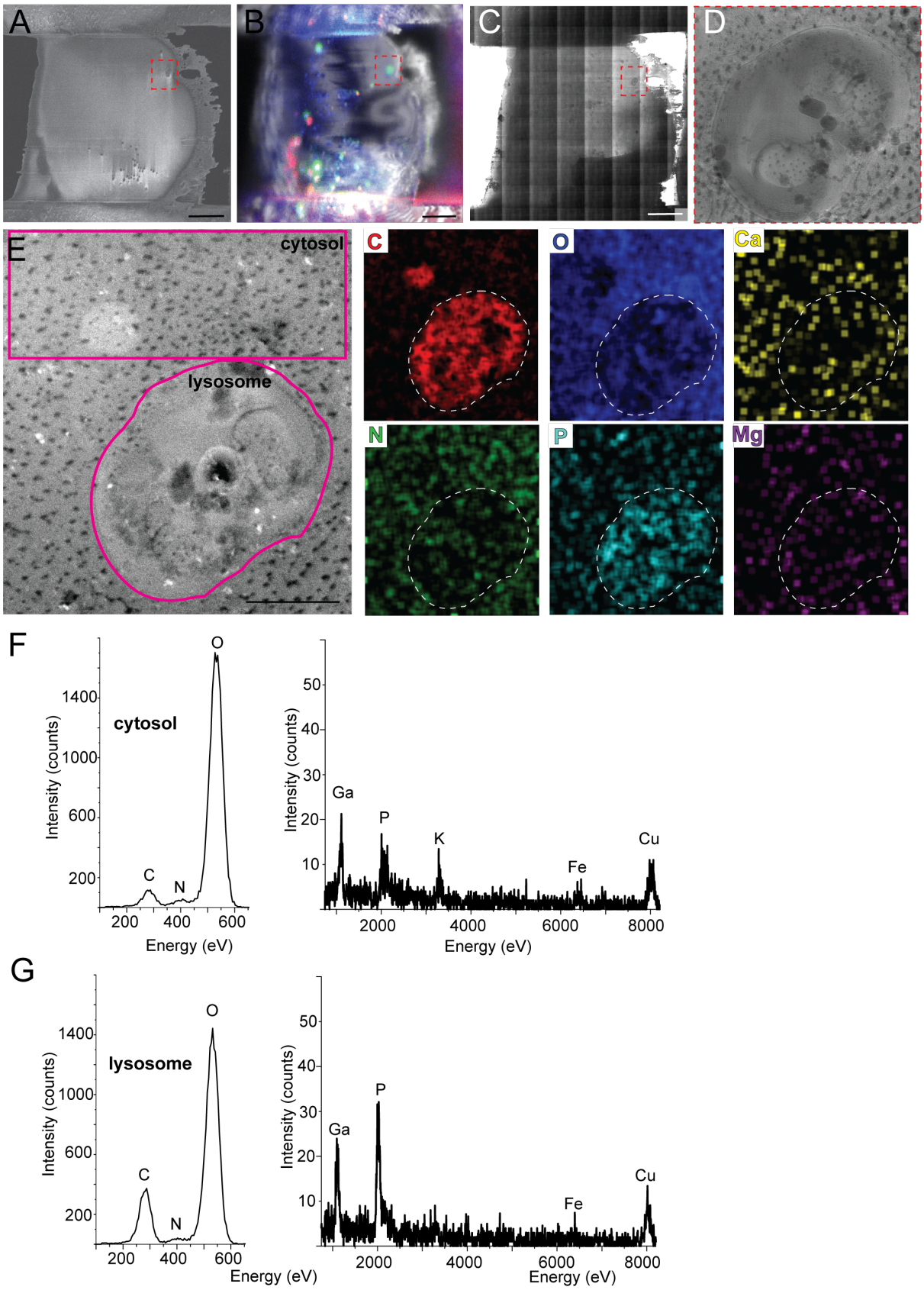

653

654 **Supplementary Figure 8: Energy-dispersive X-ray (EDX) spectroscopy**
655 **combined with STEM imaging of a lysosome.** (A) Scanning electron microscopy
656 (SEM) images of lamella with visible droplets in inset. (B) SEM image superimposed
657 with fluorescent image of green autofluorescence. (C) Overview image of
658 corresponding recorded transmission electron microscope (TEM). (D) Large vesicular
659 lysosome structure in higher magnification TEM image. (E) HAADF-STEM image of
660 lysosome corresponding elemental images of carbon (C), oxygen (O), calcium (Ca),
661 nitrogen (N), phosphorus (P) and magnesium (Mg). Scale bar 500 nm. The image
662 shows two insets of the cytosol and droplet region used for subsequent averaging.
663 EDX spectra of (F) cytosol region and (G) lysosome regions show significant gallium
664 signal originating from the FIB preparation procedure.

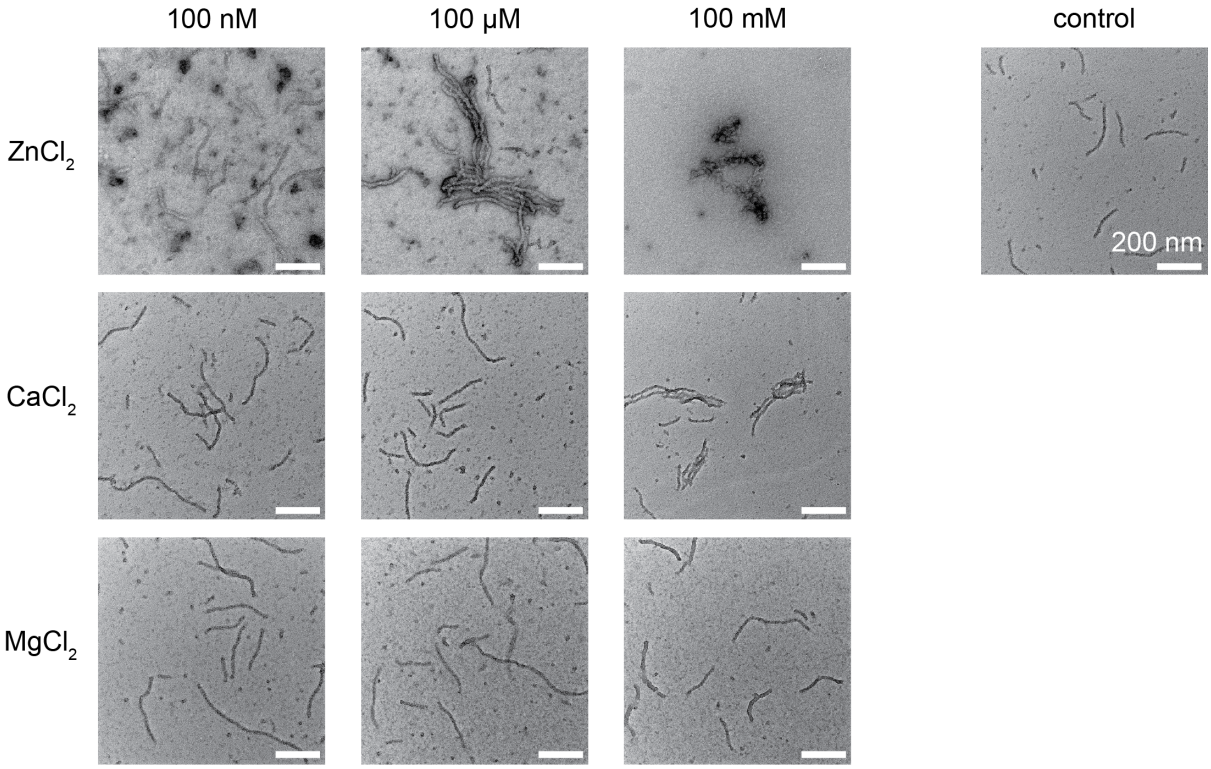

665

666 **Supplementary Figure 9: Effect of divalent cation salts on p62 filaments.** p62
667 filaments at 1 μM concentration were mixed with 100 nM, 100 μM and 100 mM of
668 $ZnCl_2$, $CaCl_2$ and $MgCl_2$, respectively. The samples were incubated for 30 minutes and
669 subsequently negatively stained. As a control, p62 filaments were mixed with desalting
670 buffer. For increasing concentrations of $ZnCl_2$from 100 μM and for $CaCl_2$ from 100 mM
671 bundling of p62 filaments was observed. For $MgCl_2$ no clear effect of bundling was
672 observed.

673

References

Abramson, J., Adler, J., Dunger, J., Evans, R., Green, T., Pritzel, A., Ronneberger, O., Willmore, L., Ballard, A. J., Bambrick, J., Bodenstein, S. W., Evans, D. A., Hung, C.-C., O'Neill, M., Reiman, D., Tunyasuvunakool, K., Wu, Z., Žemgulytė, A., Arvaniti, E., … Jumper, J. M. (2024). Accurate structure prediction of biomolecular interactions with AlphaFold 3. *Nature*, *630*(8016), 493–500. https://doi.org/10.1038/s41586-024-07487-w

Beckers, M., & Sachse, C. (2020). Permutation testing of Fourier shell correlation for resolution estimation of cryo-EM maps. *Journal of Structural Biology*, *212*(1), 107579. https://doi.org/10.1016/j.jsb.2020.107579

Berkamp, S., Daviran, D., Smeets, M., Caignard, A., Jani, R. A., Sundermeyer, P., Jonker, C., Gerlach, S., Hoffmann, B., Lau, K., & Sachse, C. (2023). Correlative Light and Electron Cryo-Microscopy Workflow Combining Micropatterning, Ice Shield, and an In-Chamber Fluorescence Light Microscope. *Bio-Protocol*, *13*(24), e4901. https://doi.org/10.21769/bioprotoc.4901

Birgisdottir, Å. B., Lamark, T., & Johansen, T. (2013). The LIR motif – crucial for selective autophagy. *Journal of Cell Science*, *126*(15), 3237–3247. https://doi.org/10.1242/jcs.126128

Bjørkøy, G., Lamark, T., Brech, A., Outzen, H., Perander, M., Øvervatn, A., Stenmark, H., & Johansen, T. (2005). p62/SQSTM1 forms protein aggregates degraded by autophagy and has a protective effect on huntingtin-induced cell death. *The Journal of Cell Biology*, *171*(4), 603–614. https://doi.org/10.1083/jcb.200507002

Brangwynne, C. P., Eckmann, C. R., Courson, D. S., Rybarska, A., Hoege, C., Gharakhani, J., Jülicher, F., & Hyman, A. A. (2009). Germline P Granules Are Liquid Droplets That Localize by Controlled Dissolution/Condensation. *Science*, *324*(5935), 1729–1732. https://doi.org/10.1126/science.1172046

Buchholz, T. O., Krull, A., Shahidi, R., Pigino, G., Jékely, G., & Jug, F. (2019). Content-aware image restoration for electron microscopy. *Methods in Cell Biology*, *152*, 277–289. https://doi.org/10.1016/bs.mcb.2019.05.001

Chen, M., Ren, X., Nguyen, T. N., Khuu, G., Cook, A. S. I., Lazarou, M., & Hurley, J. H. (2023). *Structure and activation of the human autophagy-initiating ULK1C:PI3KC3-C1 supercomplex*. https://doi.org/10.1101/2023.06.01.543278

Christian, F., Krause, E., Houslay, M. D., & Baillie, G. S. (2014). PKA phosphorylation of p62/SQSTM1 regulates PB1 domain interaction partner binding. *Biochimica Et Biophysica Acta*, *1843*(11), 2765–2774. https://doi.org/10.1016/j.bbamcr.2014.07.021

Ciani, B., Layfield, R., Cavey, J. R., Sheppard, P. W., & Searle, M. S. (2003). Structure of the Ubiquitin-associated Domain of p62 (SQSTM1) and Implications for Mutations That Cause Paget's Disease of Bone. *Journal of Biological Chemistry*, *278*(39), 37409–37412. https://doi.org/10.1074/jbc.m307416200

Ciuffa, R., Lamark, T., Tarafder, A. K., Guesdon, A., Rybina, S., Hagen, W., Johansen, T., & Sachse, C. (2015). The Selective Autophagy Receptor p62 Forms a Flexible Filamentous Helical Scaffold. *Cell Reports*, *11*(5), 748–758. https://doi.org/10.1016/j.celrep.2015.03.062

Decuypere, J.-P., Kindt, D., Luyten, T., Welkenhuyzen, K., Missiaen, L., Smedt, H. D., Bultynck, G., & Parys, J. B. (2013). mTOR-Controlled Autophagy Requires Intracellular Ca2+ Signaling. *PLoS ONE*, *8*(4), e61020. https://doi.org/10.1371/journal.pone.0061020

Desfosses, A., Ciuffa, R., Gutsche, I., & Sachse, C. (2014). SPRING – An image processing package for single-particle based helical reconstruction from electron cryomicrographs. *Journal of Structural Biology*, *185*(1), 15–26. https://doi.org/10.1016/j.jsb.2013.11.003

Dupont, N., Chauhan, S., Arko-Mensah, J., Castillo, E. F., Masedunskas, A., Weigert, R., Robenek, H., Proikas-Cezanne, T., & Deretic, V. (2014). Neutral Lipid Stores and Lipase PNPLA5 Contribute to Autophagosome Biogenesis. *Current Biology*, *24*(6), 609–620. https://doi.org/10.1016/j.cub.2014.02.008

Duran, A., Amanchy, R., Linares, J. F., Joshi, J., Abu-Baker, S., Porollo, A., Hansen, M., Moscat, J., & Diaz-Meco, M. T. (2011). p62 is a key regulator of nutrient sensing in the mTORC1 pathway. *Molecular Cell*, *44*(1), 134–146. https://doi.org/10.1016/j.molcel.2011.06.038

Feng, X., Sun, D., Li, Y., Zhang, J., Liu, S., Zhang, D., Zheng, J., Xi, Q., Liang, H., Zhao, W., Li, Y., Xu, M., He, J., Liu, T., Hasim, A., Ma, M., Xu, P., & Mi, N. (2023). Local membrane source gathering by p62 body drives autophagosome formation. *Nature Communications*, *14*(1), 7338. https://doi.org/10.1038/s41467-023-42829-8

740 Feng, Y., He, D., Yao, Z., & Klionsky, D. J. (2014). The machinery of macroautophagy.
741 *Cell Research*, *24*(1), 24–41. https://doi.org/10.1038/cr.2013.168

742 Ganeva, I., Lim, K., Boulanger, J., Hoffmann, P. C., Muriel, O., Borgeaud, A. C.,
743 Hagen, W. J. H., Savage, D. B., & Kukulski, W. (2023). The architecture of
744 Cidec-mediated interfaces between lipid droplets. *Cell Reports*, *42*(2), 112107.
745 https://doi.org/10.1016/j.celrep.2023.112107

746 Ichimura, Y., Kumanomidou, T., Sou, Y., Mizushima, T., Ezaki, J., Ueno, T., Kominami,
747 E., Yamane, T., Tanaka, K., & Komatsu, M. (2008). Structural basis for sorting
748 mechanism of p62 in selective autophagy. *The Journal of Biological Chemistry*,
749 *283*(33), 22847–22857. https://doi.org/10.1074/jbc.M802182200

750 Ichimura, Y., Waguri, S., Sou, Y.-S., Kageyama, S., Hasegawa, J., Ishimura, R., Saito,
751 T., Yang, Y., Kouno, T., Fukutomi, T., Hoshii, T., Hirao, A., Takagi, K.,
752 Mizushima, T., Motohashi, H., Lee, M.-S., Yoshimori, T., Tanaka, K.,
753 Yamamoto, M., & Komatsu, M. (2013). Phosphorylation of p62 activates the
754 Keap1-Nrf2 pathway during selective autophagy. *Molecular Cell*, *51*(5), 618–
755 631. https://doi.org/10.1016/j.molcel.2013.08.003

756 Itakura, E., & Mizushima, N. (2011). p62 targeting to the autophagosome formation
757 site requires self-oligomerization but not LC3 binding. *The Journal of Cell*
758 *Biology*, *192*(1), 17–27. https://doi.org/10.1083/jcb.201009067

759 Jakobi, A. J., Huber, S. T., Mortensen, S. A., Schultz, S. W., Palara, A., Kuhm, T.,
760 Shrestha, B. K., Lamark, T., Hagen, W. J. H., Wilmanns, M., Johansen, T.,
761 Brech, A., & Sachse, C. (2020). Structural basis of p62/SQSTM1 helical
762 filaments and their role in cellular cargo uptake. *Nature Communications*, *11*(1),
763 440. https://doi.org/10.1038/s41467-020-14343-8

764 Joung, I., Strominger, J. L., & Shin, J. (1996). Molecular cloning of a phosphotyrosine-
765 independent ligand of the p56lck SH2 domain. *Proceedings of the National*
766 *Academy of Sciences*, *93*(12), 5991–5995.
767 https://doi.org/10.1073/pnas.93.12.5991

768 Kimanius, D., Dong, L., Sharov, G., Nakane, T., & Scheres, S. H. W. (2021). New tools
769 for automated cryo-EM single-particle analysis in RELION-4.0. *Biochemical*
770 *Journal*, *478*(24), 4169–4185. https://doi.org/10.1042/BCJ20210708

771 Kirkin, V., Lamark, T., Sou, Y.-S., Bjørkøy, G., Nunn, J. L., Bruun, J.-A., Shvets, E.,
772 McEwan, D. G., Clausen, T. H., Wild, P., Bilusic, I., Theurillat, J.-P., Øvervatn,
773 A., Ishii, T., Elazar, Z., Komatsu, M., Dikic, I., & Johansen, T. (2009). A role for

774 NBR1 in autophagosomal degradation of ubiquitinated substrates. *Molecular*
775 *Cell*, *33*(4), 505–516. https://doi.org/10.1016/j.molcel.2009.01.020

776 Komatsu, M., Kurokawa, H., Waguri, S., Taguchi, K., Kobayashi, A., Ichimura, Y., Sou,
777 Y.-S., Ueno, I., Sakamoto, A., Tong, K. I., Kim, M., Nishito, Y., Iemura, S.,
778 Natsume, T., Ueno, T., Kominami, E., Motohashi, H., Tanaka, K., & Yamamoto,
779 M. (2010). The selective autophagy substrate p62 activates the stress
780 responsive transcription factor Nrf2 through inactivation of Keap1. *Nature Cell*
781 *Biology*, *12*(3), 213–223. https://doi.org/10.1038/ncb2021

782 Korfhage, J. L., Wan, N., Elhan, H., Kauffman, L., Pineda, M., Fuller, D. M., Thiam, A.
783 R., Reinisch, K. M., & Melia, T. J. (2023). *ATG2A-mediated bridge-like lipid*
784 *transport regulates lipid droplet accumulation*.
785 https://doi.org/10.1101/2023.08.14.553257

786 Kraft, L. J., Nguyen, T. A., Vogel, S. S., & Kenworthy, A. K. (2014). Size, stoichiometry,
787 and organization of soluble LC3-associated complexes. *Autophagy*, *10*(5),
788 861–877. https://doi.org/10.4161/auto.28175

789 Kroemer, G., Mariño, G., & Levine, B. (2010). Autophagy and the Integrated Stress
790 Response. *Molecular Cell*, *40*(2), 280–293.
791 https://doi.org/10.1016/j.molcel.2010.09.023

792 Kumar, S., Rechav, K., Kaplan-Ashiri, I., & Gal, A. (2020). Imaging and quantifying
793 homeostatic levels of intracellular silicon in diatoms. *Science Advances*, *6*(42),
794 eaaz7554. https://doi.org/10.1126/sciadv.aaz7554

795 Kumsta, C., Chang, J. T., Lee, R., Tan, E. P., Yang, Y., Loureiro, R., Choy, E. H., Lim,
796 S. H. Y., Saez, I., Springhorn, A., Hoppe, T., Vilchez, D., & Hansen, M. (2019).
797 The autophagy receptor p62/SQST-1 promotes proteostasis and longevity in C.
798 elegans by inducing autophagy. *Nature Communications*, *10*(1), 5648.
799 https://doi.org/10.1038/s41467-019-13540-4

800 Kwon, D. H., Park, O. H., Kim, L., Jung, Y. O., Park, Y., Jeong, H., Hyun, J., Kim, Y.
801 K., & Song, H. K. (2018). Insights into degradation mechanism of N-end rule
802 substrates by p62/SQSTM1 autophagy adapter. *Nature Communications*, *9*(1),
803 3291. https://doi.org/10.1038/s41467-018-05825-x

804 Lamark, T., Perander, M., Outzen, H., Kristiansen, K., Øvervatn, A., Michaelsen, E.,
805 Bjørkøy, G., & Johansen, T. (2003). Interaction codes within the family of
806 mammalian Phox and Bem1p domain-containing proteins. *The Journal of*

807 *Biological Chemistry*, *278*(36), 34568–34581.
808 https://doi.org/10.1074/jbc.M303221200

809 Lamm, L., Righetto, R. D., Wietrzynski, W., Pöge, M., Martinez-Sanchez, A., Peng, T.,
810 & Engel, B. D. (2022). MemBrain: A deep learning-aided pipeline for detection
811 of membrane proteins in Cryo-electron tomograms. *Computer Methods and*
812 *Programs in Biomedicine*, *224*, 106990.
813 https://doi.org/10.1016/j.cmpb.2022.106990

814 Lazarou, M., Sliter, D. A., Kane, L. A., Sarraf, S. A., Wang, C., Burman, J. L., Sideris,
815 D. P., Fogel, A. I., & Youle, R. J. (2015). The ubiquitin kinase PINK1 recruits
816 autophagy receptors to induce mitophagy. *Nature*, *524*(7565), 309–314.
817 https://doi.org/10.1038/nature14893

818 Lee, Y., Chou, T.-F., Pittman, S. K., Keith, A. L., Razani, B., & Weihl, C. C. (2017).
819 Keap1/Cullin3 Modulates p62/SQSTM1 Activity via UBA Domain
820 Ubiquitination. *Cell Reports*, *19*(1), 188–202.
821 https://doi.org/10.1016/j.celrep.2017.03.030

822 Lee, Y.-K., & Lee, J.-A. (2016). Role of the mammalian ATG8/LC3 family in autophagy:
823 differential and compensatory roles in the spatiotemporal regulation of
824 autophagy. *BMB Reports*, *49*(8), 424–430.
825 https://doi.org/10.5483/BMBRep.2016.49.8.081

826 Liu, Y.-T., Zhang, H., Wang, H., Tao, C.-L., Bi, G.-Q., & Zhou, Z. H. (2021). Isotropic
827 Reconstruction of Electron Tomograms with Deep Learning. *bioRxiv*,
828 2021.07.17.452128. https://doi.org/10.1101/2021.07.17.452128

829 MacVicar, T. D. B., Mannack, L. V. J. C., Lees, R. M., & Lane, J. D. (2015). Targeted
830 siRNA Screens Identify ER-to-Mitochondrial Calcium Exchange in Autophagy
831 and Mitophagy Responses in RPE1 Cells. *International Journal of Molecular*
832 *Sciences*, *16*(6), 13356–13380. https://doi.org/10.3390/ijms160613356

833 Mailler, E., Guardia, C. M., Bai, X., Jarnik, M., Williamson, C. D., Li, Y., Maio, N.,
834 Golden, A., & Bonifacino, J. S. (2021). The autophagy protein ATG9A enables
835 lipid mobilization from lipid droplets. *Nature Communications*, *12*(1), 6750.
836 https://doi.org/10.1038/s41467-021-26999-x

837 Man, N., Chen, Y., Zheng, F., Zhou, W., & Wen, L.-P. (2010). Induction of genuine
838 autophagy by cationic lipids in mammalian cells. *Autophagy*, *6*(4), 449–454.
839 https://doi.org/10.4161/auto.6.4.11612

840 Mastronarde, D. N. (2005). Automated electron microscope tomography using robust
841 prediction of specimen movements. *Journal of Structural Biology*, *152*(1), 36–
842 51. https://doi.org/10.1016/j.jsb.2005.07.007

843 Mastronarde, D. N., & Held, S. R. (2017). Automated tilt series alignment and
844 tomographic reconstruction in IMOD. *Journal of Structural Biology*, *197*(2),
845 102–113. https://doi.org/10.1016/j.jsb.2016.07.011

846 Mizushima, N., Yamamoto, A., Hatano, M., Kobayashi, Y., Kabeya, Y., Suzuki, K.,
847 Tokuhisa, T., Ohsumi, Y., & Yoshimori, T. (2001). Dissection of
848 Autophagosome Formation Using Apg5-Deficient Mouse Embryonic Stem
849 Cells. *The Journal of Cell Biology*, *152*(4), 657–668.
850 https://doi.org/10.1083/jcb.152.4.657

851 Mizushima, N., Yoshimori, T., & Ohsumi, Y. (2011). The Role of Atg Proteins in
852 Autophagosome Formation. *Annual Review of Cell and Developmental Biology*,
853 *27*(1), 107–132. https://doi.org/10.1146/annurev-cellbio-092910-154005

854 Mo, R. H., Zaro, J. L., Ou, J.-H. J., & Shen, W.-C. (2012). Effects of Lipofectamine
855 2000/siRNA Complexes on Autophagy in Hepatoma Cells. *Molecular*
856 *Biotechnology*, *51*(1), 1–8. https://doi.org/10.1007/s12033-011-9422-6

857 Morin, A., Eisenbraun, B., Key, J., Sanschagrin, P. C., Timony, M. A., Ottaviano, M.,
858 & Sliz, P. (2013). Cutting Edge: Collaboration gets the most out of software.
859 *eLife*, *2*, e01456. https://doi.org/10.7554/eLife.01456

860 Morishita, H., Eguchi, S., Kimura, H., Sasaki, J., Sakamaki, Y., Robinson, M. L.,
861 Sasaki, T., & Mizushima, N. (2013). Deletion of Autophagy-related 5 (Atg5) and
862 Pik3c3 Genes in the Lens Causes Cataract Independent of Programmed
863 Organelle Degradation. *Journal of Biological Chemistry*, *288*(16), 11436–
864 11447. https://doi.org/10.1074/jbc.M112.437103

865 Nakatogawa, H., Suzuki, K., Kamada, Y., & Ohsumi, Y. (2009). Dynamics and diversity
866 in autophagy mechanisms: lessons from yeast. *Nature Reviews Molecular Cell*
867 *Biology*, *10*(7), 458–467. https://doi.org/10.1038/nrm2708

868 Omrane, M., M'Barek, K. B., Santinho, A., Nguyen, N., Nag, S., Melia, T. J., & Thiam,
869 A. R. (2023). LC3B is lipidated to large lipid droplets during prolonged starvation
870 for noncanonical autophagy. *Developmental Cell*, *58*(14), 1266–1281.e7.
871 https://doi.org/10.1016/j.devcel.2023.05.009

872 Otomo, C., Metlagel, Z., Takaesu, G., & Otomo, T. (2013). Structure of the human
873 ATG12 conjugate required for LC3 lipidation in autophagy. *Nature Structural &*
874 *Molecular Biology*, *20*(1), 59–66. https://doi.org/10.1038/nsmb.2431

875 Pankiv, S., Clausen, T., Lamark, T., Brech, A., Bruun, J.-A., Outzen, H., Øvervatn, A.,
876 Bjørkøy, G., & Johansen, T. (2007). p62/SQSTM1 Binds Directly to Atg8/LC3
877 to Facilitate Degradation of Ubiquitinated Protein Aggregates by Autophagy.
878 *Journal of Biological Chemistry*, *282*(33), 24131–24145.
879 https://doi.org/10.1074/jbc.m702824200

880 Pettersen, E. F., Goddard, T. D., Huang, C. C., Couch, G. S., Greenblatt, D. M., Meng,
881 E. C., & Ferrin, T. E. (2004). UCSF Chimera—A visualization system for
882 exploratory research and analysis. *Journal of Computational Chemistry*, *25*(13),
883 1605–1612. https://doi.org/10.1002/jcc.20084

884 Puissant, A., Fenouille, N., & Auberger, P. (2012). When autophagy meets cancer
885 through P62/SQSTM1. *American Journal of Cancer Research*, *2*(4), 397–413.

886 Punjani, A., Rubinstein, J. L., Fleet, D. J., & Brubaker, M. A. (2017). cryoSPARC:
887 algorithms for rapid unsupervised cryo-EM structure determination. *Nature*
888 *Methods*, *14*(3), 290–296. https://doi.org/10.1038/nmeth.4169

889 Puri, C., Renna, M., Bento, Carla F., Moreau, K., & Rubinsztein, David C. (2013).
890 Diverse Autophagosome Membrane Sources Coalesce in Recycling
891 Endosomes. *Cell*, *154*(6), 1285–1299.
892 https://doi.org/10.1016/j.cell.2013.08.044

893 Robichaud, S., Fairman, G., Vijithakumar, V., Mak, E., Cook, D. P., Pelletier, A. R.,
894 Huard, S., Vanderhyden, B. C., Figeys, D., Lavallée-Adam, M., Baetz, K., &
895 Ouimet, M. (2021). Identification of novel lipid droplet factors that regulate
896 lipophagy and cholesterol efflux in macrophage foam cells. *Autophagy*, *17*(11),
897 3671–3689. https://doi.org/10.1080/15548627.2021.1886839

898 Rogov, V., Dötsch, V., Johansen, T., & Kirkin, V. (2014). Interactions between
899 Autophagy Receptors and Ubiquitin-like Proteins Form the Molecular Basis for
900 Selective Autophagy. *Molecular Cell*, *53*(2), 167–178.
901 https://doi.org/10.1016/j.molcel.2013.12.014

902 Rohou, A., & Grigorieff, N. (2015). CTFFIND4: Fast and accurate defocus estimation
903 from electron micrographs. *Journal of Structural Biology*, *192*(2), 216–221.
904 https://doi.org/10.1016/j.jsb.2015.08.008

905 Rosenthal, P. B., & Henderson, R. (2003). Optimal Determination of Particle
906 Orientation, Absolute Hand, and Contrast Loss in Single-particle Electron
907 Cryomicroscopy. *Journal of Molecular Biology*, *333*(4), 721–745.
908 https://doi.org/10.1016/j.jmb.2003.07.013

909 Scheres, S. H. W. (2012). RELION: Implementation of a Bayesian approach to cryo-
910 EM structure determination. *Journal of Structural Biology*, *180*(3), 519–530.
911 https://doi.org/https://doi.org/10.1016/j.jsb.2012.09.006

912 Schindelin, J., Arganda-Carreras, I., Frise, E., Kaynig, V., Longair, M., Pietzsch, T.,
913 Preibisch, S., Rueden, C., Saalfeld, S., Schmid, B., Tinevez, J.-Y., White, D. J.,
914 Hartenstein, V., Eliceiri, K., Tomancak, P., & Cardona, A. (2012). Fiji: an open-
915 source platform for biological-image analysis. *Nature Methods*, *9*(7), 676.
916 https://doi.org/10.1038/nmeth.2019

917 Schott, M. B., Weller, S. G., Schulze, R. J., Krueger, E. W., Drizyte-Miller, K., Casey,
918 C. A., & McNiven, M. A. (2019). Lipid droplet size directs lipolysis and lipophagy
919 catabolism in hepatocytes. *Journal of Cell Biology*, *218*(10), 3320–3335.
920 https://doi.org/10.1083/jcb.201803153

921 Shpilka, T., Weidberg, H., Pietrokovski, S., & Elazar, Z. (2011). Atg8: an autophagy-
922 related ubiquitin-like protein family. *Genome Biology*, *12*(7), 226.
923 https://doi.org/10.1186/gb-2011-12-7-226

924 Shpilka, T., Welter, E., Borovsky, N., Amar, N., Mari, M., Reggiori, F., & Elazar, Z.
925 (2015). Lipid droplets and their component triglycerides and steryl esters
926 regulate autophagosome biogenesis. *The EMBO Journal*, *34*(16), 2117–2131.
927 https://doi.org/10.15252/embj.201490315

928 Singh, R., Kaushik, S., Wang, Y., Xiang, Y., Novak, I., Komatsu, M., Tanaka, K.,
929 Cuervo, A. M., & Czaja, M. J. (2009). Autophagy regulates lipid metabolism.
930 *Nature*, *458*(7242), 1131–1135. https://doi.org/10.1038/nature07976

931 Smeets, M., Bieber, A., Capitanio, C., Schioetz, O., van der Heijden, T., Effting, A.,
932 Piel, É., Lazem, B., Erdmann, P., & Plitzko, J. (2021). Integrated Cryo-
933 Correlative Microscopy for Targeted Structural Investigation In Situ. *Microscopy*
934 *Today*, *29*(6), 20–25. https://doi.org/10.1017/S1551929521001280

935 Stirling, D. R., Swain-Bowden, M. J., Lucas, A. M., Carpenter, A. E., Cimini, B. A., &
936 Goodman, A. (2021). CellProfiler 4: improvements in speed, utility and usability.
937 *BMC Bioinformatics*, *22*(1), 433. https://doi.org/10.1186/s12859-021-04344-9

Sun, D., Wu, R., Li, P., & Yu, L. (2019). Phase Separation in Regulation of Aggrephagy. *Journal of Molecular Biology*, *432*(1), 160–169. https://doi.org/10.1016/j.jmb.2019.06.026

Sun, D., Wu, R., Zheng, J., Li, P., & Yu, L. (2018). Polyubiquitin chain-induced p62 phase separation drives autophagic cargo segregation. *Cell Research*, *28*(4), 405–415. https://doi.org/10.1038/s41422-018-0017-7

Tegunov, D., & Cramer, P. (2019). Real-time cryo-electron microscopy data preprocessing with Warp. *Nature Methods*, *16*(11), 1146–1152. https://doi.org/10.1038/s41592-019-0580-y

Thörnig, P. (2021). JURECA: Data Centric and Booster Modules implementing the Modular Supercomputing Architecture at Jülich Supercomputing Centre. *Journal of Large-Scale Research Facilities*, *7*. https://doi.org/https://doi.org/10.17815/jlsrf-7-182

Toro-Nahuelpan, M., Zagoriy, I., Senger, F., Blanchoin, L., Théry, M., & Mahamid, J. (2019). Tailoring cryo-electron microscopy grids by photo-micropatterning for in-cell structural studies. *bioRxiv*, 676189. https://doi.org/10.1101/676189

Tsai, T.-H., Chen, E., Li, L., Saha, P., Lee, H.-J., Huang, L.-S., Shelness, G. S., Chan, L., & Chang, B. H.-J. (2017). The constitutive lipid droplet protein PLIN2 regulates autophagy in liver. *Autophagy*, *13*(7), 1130–1144. https://doi.org/10.1080/15548627.2017.1319544

Turco, E., Savova, A., Gere, F., Ferrari, L., Romanov, J., Schuschnig, M., & Martens, S. (2021). Reconstitution defines the roles of p62, NBR1 and TAX1BP1 in ubiquitin condensate formation and autophagy initiation. *Nature Communications*, *12*(1), 5212. https://doi.org/10.1038/s41467-021-25572-w

Turco, E., Witt, M., Abert, C., Bock-Bierbaum, T., Su, M.-Y., Trapannone, R., Sztacho, M., Danieli, A., Shi, X., Zaffagnini, G., Gamper, A., Schuschnig, M., Fracchiolla, D., Bernklau, D., Romanov, J., Hartl, M., Hurley, J. H., Daumke, O., & Martens, S. (2019). FIP200 Claw Domain Binding to p62 Promotes Autophagosome Formation at Ubiquitin Condensates. *Molecular Cell*, *74*(Acta Crystallogr. D Biol. Crystallogr. 66 2010), 330–346.e11. https://doi.org/10.1016/j.molcel.2019.01.035

Wagner, T., Merino, F., Stabrin, M., Moriya, T., Antoni, C., Apelbaum, A., Hagel, P., Sitsel, O., Raisch, T., Prumbaum, D., Quentin, D., Roderer, D., Tacke, S., Siebolds, B., Schubert, E., Shaikh, T. R., Lill, P., Gatsogiannis, C., & Raunser,

S. (2019). SPHIRE-crYOLO is a fast and accurate fully automated particle picker for cryo-EM. *Communications Biology*, *2*(1), 218. https://doi.org/10.1038/s42003-019-0437-z

Wang, L., Zhou, J., Yan, S., Lei, G., Lee, C.-H., & Yin, X.-M. (2017). Ethanol-triggered Lipophagy Requires SQSTM1 in AML12 Hepatic Cells. *Scientific Reports*, *7*(1), 12307. https://doi.org/10.1038/s41598-017-12485-2

Wang, Y., Dahmane, S., Ti, R., Mai, X., Zhu, L., Carlson, L.-A., & Stjepanovic, G. (2024). Structural basis for lipid transfer by the ATG2A–ATG9A complex. *Nature Structural & Molecular Biology*. https://doi.org/10.1038/s41594-024-01376-6

Watson, J. D., & Crick, F. H. (1953). Molecular structure of nucleic acids; a structure for deoxyribose nucleic acid. *Nature*, *171*(4356), 737–738. https://doi.org/10.1038/171737a0

Wen, X., & Klionsky, D. J. (2016). An overview of macroautophagy in yeast. *Journal of Molecular Biology*, *428*(9), 1681–1699. https://doi.org/10.1016/j.jmb.2016.02.021

Wolf, S. G., Mutsafi, Y., Dadosh, T., Ilani, T., Lansky, Z., Horowitz, B., Rubin, S., Elbaum, M., & Fass, D. (2017). 3D visualization of mitochondrial solid-phase calcium stores in whole cells. *eLife*, *6*, e29929. https://doi.org/10.7554/elife.29929

WOLF, S. G., REZ, P., & ELBAUM, M. (2015). Phosphorus detection in vitrified bacteria by cryo-STEM annular dark-field analysis. *Journal of Microscopy*, *260*(2), 227–233. https://doi.org/10.1111/jmi.12289

Xie, Z., & Klionsky, D. J. (2007). Autophagosome formation: core machinery and adaptations. *Nature Cell Biology*, *9*(10), 1102–1109. https://doi.org/10.1038/ncb1007-1102

Yamamoto, H., Kakuta, S., Watanabe, T. M., Kitamura, A., Sekito, T., Kondo-Kakuta, C., Ichikawa, R., Kinjo, M., & Ohsumi, Y. (2012). Atg9 vesicles are an important membrane source during early steps of autophagosome formation. *Journal of Cell Biology*, *198*(2), 219–233. https://doi.org/10.1083/jcb.201202061

Yan, Y., Wang, H., Wei, C., Xiang, Y., Liang, X., Phang, C.-W., & Jiao, R. (2019). HDAC6 regulates lipid droplet turnover in response to nutrient deprivation via

1004 p62-mediated selective autophagy. *Journal of Genetics and Genomics*, *46*(4),
1005 221–229. https://doi.org/10.1016/j.jgg.2019.03.008

1006 Yao, W., Chen, Y., Zhang, Y., Zhong, S., Ye, M., Chen, Y., Fan, S., Ye, M., Yang, H.,
1007 Li, Y., Wu, C., Fan, M., Feng, S., He, Z., Zhou, L., Zhang, L., Wang, Y., Liu, W.,
1008 Tong, J., … Yi, C. (2024). Ca2+-triggered Atg11-Bmh1/2-Snf1 complex
1009 assembly initiates autophagy upon glucose starvation. *The Journal of Cell*
1010 *Biology*, *223*(9), e202310049. https://doi.org/10.1083/jcb.202310049

1011 Zaffagnini, G., Savova, A., Danieli, A., Romanov, J., Tremel, S., Ebner, M.,
1012 Peterbauer, T., Sztacho, M., Trapannone, R., Tarafder, A. K., Sachse, C., &
1013 Martens, S. (2018a). P62 filaments capture and present ubiquitinated cargos
1014 for autophagy. *The EMBO Journal*, *37*(5), e98308.
1015 https://doi.org/10.15252/embj.201798308

1016 Zaffagnini, G., Savova, A., Danieli, A., Romanov, J., Tremel, S., Ebner, M.,
1017 Peterbauer, T., Sztacho, M., Trapannone, R., Tarafder, A. K., Sachse, C., &
1018 Martens, S. (2018b). Phasing out the bad-How SQSTM1/p62 sequesters
1019 ubiquitinated proteins for degradation by autophagy. *Autophagy*, *14*(7), 1280–
1020 1282. https://doi.org/10.1080/15548627.2018.1462079

1021 Zhang, J., Tripathi, D. N., Jing, J., Alexander, A., Kim, J., Powell, R. T., Dere, R., Tait-
1022 Mulder, J., Lee, J.-H., Paull, T. T., Pandita, R. K., Charaka, V. K., Pandita, T.
1023 K., Kastan, M. B., & Walker, C. L. (2015). ATM functions at the peroxisome to
1024 induce pexophagy in response to ROS. *Nature Cell Biology*, *17*(10), 1259–
1025 1269. https://doi.org/10.1038/ncb3230

1026 Zheng, Q., Chen, Y., Chen, D., Zhao, H., Feng, Y., Meng, Q., Zhao, Y., & Zhang, H.
1027 (2022). Calcium transients on the ER surface trigger liquid-liquid phase
1028 separation of FIP200 to specify autophagosome initiation sites. *Cell*.
1029 https://doi.org/10.1016/j.cell.2022.09.001

1030 Zheng, S., Wolff, G., Greenan, G., Chen, Z., Faas, F. G. A., Bárcena, M., Koster, A.
1031 J., Cheng, Y., & Agard, D. A. (2022). AreTomo: An integrated software package
1032 for automated marker-free, motion-corrected cryo-electron tomographic
1033 alignment and reconstruction. *Journal of Structural Biology: X*, *6*, 100068.
1034 https://doi.org/10.1016/j.yjsbx.2022.100068

1035 Zierold, K., Schäfer, D., & Pietruschka, F. (1984). The element distribution in ultrathin
1036 cryosections of cultivated fibroblast cells. *Histochemistry*, *80*(4), 333–337.
1037 https://doi.org/10.1007/bf00495413

1038

1039 # Materials & Methods

1040 ## Protein expression, purification of p62, 4x-linear-ubiquitin and LC3B

1041 Full-length p62 (440 residues) was cloned into a pETM43 expression vector containing
1042 an N-terminal maltose-binding-protein (MBP) tag and a C-terminal His-tag. Both tags
1043 featured a recognition sequence for HRV-3C protease, facilitating their removal after
1044 purification. 4x-linear-Ubiquitin, CFP-LC3B, and LC3B with an additional C-terminal
1045 cysteine residue were cloned into pGEX expression vector containing an N-terminal
1046 Glutathione-S-Transferase (GST) tag with HRV-3C protease cleavage site. For protein
1047 expression E. *coli* BL21 (DE3) cells were used, with bacterial cultures grown at 37°C
1048 in Terrific Broth (TB) medium to an OD_{600} of ~2. Induction with
1049 IsoPropylThioGalactoside (IPTG) followed and cells were left to grow overnight at
1050 23°C. Cells were harvested and the pellet was stored at -80 °C until further use.

1051 After thawing on ice, cells were resuspended in lysis buffer [50 mM HEPES, pH 8.0,
1052 300 mM NaCl, 2.5 mM $MgSO_4$, 10 µM $ZnCl_2$, 0.5 mM TCEP and 1 tablet EDTA-free
1053 protease inhibitor cocktail] and lysed using a cell disruptor at 1.85 bar. Cell debris was
1054 removed by centrifugation and the cleared lysate was applied to a Ni-NTA affinity
1055 column. The column was washed twice with lysis buffer containing 10 mM and 20 mM
1056 imidazole, respectively, and protein was eluted with lysis buffer containing 300 mM
1057 imidazole. Eluted protein fractions were pooled and subsequently applied to an
1058 amylose resin that binds MBP-fusion proteins with high affinity. The column was
1059 washed with lysis buffer and the protein was eluted with lysis buffer containing 25 mM
1060 maltose. Eluted protein fractions were pooled, and buffer was exchanged to desalting
1061 buffer [50 mM HEPES, pH 8.0, 300 mM NaCl and 0.5 mM TCEP] using Zeba desalting
1062 columns.

1063 For the purification of LC3b and GST-4xUb, the cell pellets were resuspended in lysis
1064 buffer [50 mM HEPES, pH 7.4, 300 mM NaCl, 1 mM DTT, and 1 tablet EDTA-free
1065 protease inhibitor cocktail] and lysed using a cell disruptor at 1.9 bar. The cleared
1066 lysate was applied to Glutathione Sepharose 4 Fast Flow GST-tagged protein
1067 purification resin (Cytiva, Cat No 17513201), washed with 10 column volume lysis
1068 buffer, and eluted in lysis buffer containing 10 mM reduced glutathione. Elution
1069 fractions containing the protein of interested were pooled, further purified by size
1070 exclusion chromatography via SD200 16/600 column (Cytiva) [in 50 mM HEPES, pH
1071 7.4, 150 mM NaCl, 1 mM DTT], and frozen at -80°C for storage.

1072 **p62 filament formation and labeling**

1073 Protein was concentrated to approximately 2 mg/mL using a 30 kDa Amicon
1074 concentrator and subsequently incubated with 1:2.5 mass ratio of GST-HRV-3C
1075 protease for 3 h at room temperature and overnight at 4°C to remove the MBP and
1076 His-tag, allowing p62 filament formation. Filaments were isolated by centrifugation at
1077 20,000 x g for 30 min and resuspended in desalting buffer. Isolated filaments were
1078 labeled to lysine residues by incubating with 1:1 molar ratio of Cy5-NHS for 1 h at
1079 room temperature and overnight at 4°C. Excess dye was removed by centrifugation,
1080 labeled filaments were resuspended in storage buffer [50 mM HEPES, pH 8.0, 50 mM
1081 NaCl and 0.5 mM TCEP] and stored at 4°C until further use.

1082 **Cryo-EM structure determination of p62 filaments**

1083 Quantifoil Cu 200 mesh R1.2/R1.3 were glow discharged, and 2-5µL of the protein
1084 sample was applied in a Vitrobot mark IV (ThermoFischer Scientific). The sample
1085 chamber was maintained at 70-100 % humidity and 4-10 °C, with a 2-6 s blotting time
1086 before plunging into ethane/propane mixture. Data collection was performed using
1087 SerialEM(Mastronarde, 2005) on a Talos Arctica 200 KeV G2 transmission electron
1088 microscope (ThermoFischer Scientific), equipped with a K3 direct electron detector
1089 camera and Quantum GIF filter (Gatan, Inc). Approximately 4000 micrographs were
1090 collected in counted superresolution mode at 100,000x magnification with an
1091 underfocus range of -0.5 µm to -3 µm. The micrographs were motion corrected in
1092 WARP(Tegunov & Cramer, 2019) and particles were picked using the deep-learning
1093 based object detection software crYOLO (Wagner et al., 2019). Initially, the picked
1094 particle locations and micrographs were imported into RELION and
1095 SPRING(Desfosses et al., 2014; Scheres, 2012) that used CTFFIND4 for CTF
1096 estimation(Rohou & Grigorieff, 2015). Later, CTF corrected micrographs were
1097 imported in cryoSPARC (Punjani et al., 2017) and particle locations were extracted
1098 with a 90 % overlap yielding approximately 1,000,000 segments of a box size of 503
1099 Å. Two rounds of 2D classification were performed in order to remove heterogeneous
1100 particles. Classes with clearly defined PB1 domains were then selected, leading to a
1101 total of 600,000 segments. The helical parameters as determined by Jakobi et al.
1102 (Jakobi et al., 2020) of truncated p62 helical filaments were taken as starting conditions
1103 for helical refinement in cryoSPARC, where the symmetry parameters converged. The
1104 final resolution was estimated by FSC using the 0.143 cutoff(Rosenthal & Henderson,
1105 2003) and FDR-FSC criterion(Beckers & Sachse, 2020). Maps were rendered in
1106 UCSF ChimeraX (Pettersen et al., 2004).

1107 ## Single-particle fluorescence imaging in TIRF mode

1108 Surface imaging was performed with an inverted microscope (Olympus IX-81,
1109 Olympus Corp., Shinjuku, Japan) in total internal reflection fluorescence (TIRF) mode.
1110 Molecules were excited using lasers at 488 and 639 nm (Sapphire 488-200 and Obis
1111 637-140, Coherent Inc.) focused off-axis into the back-focal plane of an oil-immersion
1112 objective (Olympus UApoN, 100x, NA=1.49, Olympus Corp). The excitation power and
1113 corresponding intensity at the sample stage were 3.25 mW and 10.2 W/cm^2 for the
1114 blue laser, and 2.2 mW and 6.8 W/cm^2 for the red laser. The imaging was performed
1115 on an EMCCD camera (Andor iXon Ultra 888, Andor Technology) with 50, 100, 40 and
1116 100 ms exposure time for Supplementary Videos 1-4, corresponding to 20, 10, 25 and
1117 10 fps. Midway through acquiring Supplementary Video 2, the illumination was
1118 switched from blue to red laser to observe the same p62 filament with LC3b bound to
1119 it. Each video consists of 200 frames. Image analysis and video processing were
1120 carried out using Fiji (ImageJ, version 2.14.0) (Schindelin et al., 2012). The emitted
1121 fluorescence was collected with the same objective (objective based TIRF) and
1122 passed through a dual-band dichroic mirror as well as a dual-band emission filter
1123 (ZT488/640rpc and ZET488/640m, Chroma Technology Corp). p62 filaments-Cy5 and
1124 CFP-LC3b were diluted to concentrations of a few nM, and mixed in a 1:1 molar ratio.
1125 GST-4xUb was added at a concentration of 5 μM.

1126 ## Negative staining electron microscopy

1127 For negative staining, 3.5 μL of the sample was applied onto glow-discharged carbon-
1128 formvar-coated 300-mesh copper grids and allowed to absorb for 2 min before blotted
1129 according to the side-blotting method. The sample was subsequently stained for 30 s
1130 with 6 μL 2% uranyl acetate, blotted and allowed to dry. Negatively stained samples
1131 were examined on a Talos L120C G2 transmission electron microscope
1132 (ThermoFisher Scientific), operated at 120 kV. Micrographs at high magnification
1133 (45,000x and 92,000x) were collected on a 4k x 4k Ceta 16M CEMOS camera using
1134 TEM Imaging & Analysis Software (TIA, ThermoFisher Scientific).

1135 ## Cryo-electron tomography of reconstituted p62 filaments

1136 p62 filament cryo-EM grids were prepared as described above. Tilt series were
1137 recorded on a 200 kV Talos Arctica G2 transmission electron microscope
1138 (ThermoFisher Scientific), equipped with a Bioquantum GIF (Gatan, Inc) a Volta Phase
1139 Plate and a K3 direct electron detector (Gatan, Inc) using SerialEM (Mastronarde,
1140 2005). Each tilt was recorded as movie at 63.000x magnification with a 0.681 Å/pixel
1141 size in super resolution mode and a dose of approximately 2.0 e/Å^2/tilt, 10 frames per

1142 tilt, and a total dose per tilt series of approximately 130 e/Å^2. All tilt series were
1143 recorded from -54° to 54° with 3° increments, using a dose-symmetric bidirectional
1144 acquisition scheme and a nominal defocus of -1.2 µm. The raw data was motion
1145 corrected and CTF corrected using WARP (version 1.0.9)(Tegunov & Cramer, 2019)
1146 and the tilt series were reconstructed using IMOD(Mastronarde & Held, 2017).

1147 GST-4x-linear-Ubiquitin and p62 filaments were prepared as described above. 15 μM
1148 of GST-4x-linear-Ubiquitin were mixed with 1 μM p62 filaments. After 4 minutes
1149 incubation time at 4°C, the formed phase separation droplets were negatively stained
1150 as described above or plunge frozen with a Vitrobot Mark IV (ThermoFisher Scientific).
1151 50 nm SUVs were prepared containing 5% DSPE-PEG(2000) maleimide (Avanti Polar
1152 lipids, Cat No 880126) in DOPS (Avantiv Polar lipids, Cat No 840035). The liposomes
1153 were incubated with 100 μM LC3b-Cys for 16 h at 4°C before removing unbound
1154 LC3b-Cys by size exclusion chromatography on Sepharcyl S-500 at Äkta Micro
1155 (Cytiva). A total of 2 mg/ml of liposomes were mixed with 1 μM p62 filaments and
1156 incubated for 5 min at 4 °C. The sample was plunge frozen at a Leica GM2 plunge
1157 freezer (Leica). Tomograms were collected at a Titan Krios 300 keV TEM equipped
1158 with an BioContinuum energy filter and K3 camera at 64,000x using Tomo5 software
1159 (ThermoFisher Scientific). The tilt series were recorded from -60° to 60° with a 3°
1160 increment in a dose-symmetric bidirectional acquisition scheme. An electron dose of
1161 4.0 e^-/Å^2/tilt with 6 frames per tilt, resulted in a total dose per tilt series of approximately
1162 160 e^-/Å^2. The defocus was varied between -2.0 to -4.0 µm. The images were motion
1163 corrected in WARP (Tegunov & Cramer, 2019) and tomograms reconstructed with
1164 AreTomo (S. Zheng et al., 2022). Overall binning was 16x and resulted in a pixel size
1165 of 11.2 Å. Tomograms were denoised and missing wedge corrected with IsoNet (Liu
1166 et al., 2021).

1167 Cell culture and transfection

1168 Cell culture experiments were carried out in human RPE1 cells (hTERT RPE1, CRL-
1169 4000, ATCC) cultured at 37°C and 5% CO_2 in DMEM GlutaMAX media (Gibco, Cat
1170 No 31331028) supplemented with 10% FCS (Sigma-Aldrich, Cat No F7524) and
1171 Pen/Strep (Gibco, Cat No 15140122). For confocal microscopy experiments prior to
1172 plunge-freezing, the culturing media was substituted with media of low fluorescence
1173 background; Fluorobrite DMEM (Gibco, Cat No A1896701). Additional experiments
1174 were performed on RPE1 cells stably expressing human mCherry-p62. Transient
1175 expression of mCherry-p62 was executed by transfection with FugeneHD (Promega,
1176 Cat No E2311) and a modified pDEST vector containing the human wildtype p62 gene
1177 fused with an N-terminal mCherry sequence (Pankiv et al., 2007). Knockdown

1178 experiments were carried out by transfection with RNAiMAX (ThermoFisher, Cat No
1179 13778075) and ON-TARGETplus SMARTpool siRNA against ATG5 (Dharmcon
1180 Horizon Discovery, Cat No L-004374-00-0005), GADPH (Dharmcon Horizon
1181 Discovery, Cat No D-001830-10-05) and a non-targeting control (Dharmcon Horizon
1182 Discovery, Cat No D-001810-10-05). Follow-up experiments were performed 72 hours
1183 after a reverse transfection with 75 nm siRNA. Lipid droplets were stained with 1:500
1184 Lipi-Blue (Dojindo, Cat No LD01-10) for 24 hours. Lysosomes were stained with the
1185 CytoPainter Lysosomal staining kit (Abcam, Cat No ab112136).

1186 Western Blot

1187 Cells were lysed by a quick wash with ice cold PBS (Gibco, Cat No 10010056) and a
1188 subsequent 15 min incubation in ice cold RIPA buffer (Sigma-Aldrich, Cat No R0278-
1189 50mL) supplemented with a protease inhibitor cocktail (Roche, Cat No 11836170001).
1190 Cell lysate was collected with a cell scraper before removing the cell debris by
1191 centrifugation. Total protein content was quantified and corrected using a Pierce 660
1192 nm assay (ThermoFisher, Cat No 22662) before boiling the sampling in a reducing
1193 sample buffer and separation on a 4-15 % mini-PROTEAN Precast SDS-PAGE (Bio-
1194 Rad, Cat No 4561085). Transfer to PVDF membrane was performed using a Trans-
1195 Blot pack (Bio-Rad, Cat No 1704156) and the membrane was blocked for 2 h in 2 %
1196 BSA in TBST at 4 °C. The membrane was incubated overnight with primary antibody
1197 in 1 % BSA in TBST at 4 °C, washed 3 times in TBST before the secondary antibody
1198 was added for 2 h in 1 % BSA in TBST at 4 °C. Prior to imaging on the Azure Sapphire
1199 RGB Biomolecular Imager (Azure Biosystems), the membrane was washed 3 times in
1200 TBST and incubated in Azure Radiance Q HRP (Biozym, Cat No 512101). The
1201 following antibodies were used: polyclonal rabbit anti-p62 (MBL International, Cat No
1202 PM045), monoclonal rabbit anti-ATG5 (Abcam, Cat No ab108327), monoclonal mouse
1203 anti-GADPH (Invitrogen, Cat No MA1-16757), polyclonal rabbit anti-LC3 (Abcam, Cat
1204 No ab48394), goat anti-mouse HRP conjugate (ThermoFisher Cat No 32230), and
1205 goat anti-rabbit HRP conjugate (ThermoFisher, Cat No 31460). Band intensity
1206 quantifications were performed using ImageLab (BioRad, version 6.1.0).

1207 Cellular tomography grid preparation

1208 RPE1 Cells were seeded on micropatterned grids before plunge freezing, For a more
1209 detailed protocol see Berkamp et al. Bio-Protocols 2023 (Berkamp et al., 2023; Toro-
1210 Nahuelpan et al., 2019). Briefly, 200 mesh gold Quantifoil R2/1 grids with a SiO_2
1211 support layer (Quantifoil, Cat No N1-S15nAu20-01) were glow discharged and treated
1212 with PLL-g-PEG (SuSoS, PLL(20)-g[3.5]- PEG(5)) overnight. Next, the grids were

1213 washed in PBS and placed in drops of 14.5 mg/mL PLPP (Alvéole, Cat No PLPP) and
1214 20 µm circles in the center of 10x10 grid squares were micropatterned with a PRIMO
1215 photopatterning device (Alvéole, Photopatterning Device consisting of a DMD + laser
1216 375 nm, 75 mW module, and driving electronics). The grids were then washed
1217 thoroughly in PBS and incubated in human fibronectin immediately before use (Gibco,
1218 Cat No PHE0023). The cells were trypsinized (Gibco, Cat No 25300054), passed
1219 through a 40 µm cell strainer (PluriSelect, Cat No 43-10040-40) and counted before
1220 seeding ~200,000 cells in a 30 mm glass-bottom dish (Greiner Bio-One, Cat No
1221 627860) containing the micropatterned grids in a small amount of DMEM. The cells
1222 were allowed to attach to the grids for 4-5 h before vitrification in liquid ethane using a
1223 Vitrobot Mark IV (ThermoFisher Scientific). The following settings were used; a
1224 chamber temperature of 37 °C, a chamber humidity of 85 % humidity, backside blotting
1225 with a 8.5 s blot time and blot force of -10 and a drain time of 1 s.

1226 Confocal microscopy

1227 RPE1 cell phenotypes were studied using a Zeiss LSM710 laser scanning confocal
1228 microscope (Carl Zeiss GmbH). The cells were grown in 30 mm glass bottom dishes
1229 with 4 compartments (Greiner Bio-One, Cat No 627870) and imaged at 37°C using a
1230 Zeiss 63× oil immersion objective (Plan-Apochromat, DIC, 1.4 NA). Lipi-Blue was
1231 excited with a diode laser at 405 nm and fluorescent emission was detected after
1232 passing a suitable emission filter (410-500 nm) using a Multi Alkali photomultiplier
1233 tube. The lysosomal stain was excited using an argon ion laser at 488 nm and
1234 emission was detected using an emission filter (499-541 nm). MCherry-p62 was
1235 detected using a 543 HeNe543 laser and an emission filter set to 579-696 nm using a
1236 GaAsP photomultiplier tube. Image analysis and quantification were done using Fiji
1237 (ImageJ, version 2.14.0) (Schindelin et al., 2012) and a self-written routine in
1238 CellProfiler (version 4.2.6) (Stirling et al., 2021). Measurements were exported as .csv
1239 files and analyzed in OriginPro 2023 (OriginLab Corporation, version 10.0.0.154).
1240 Vitrified grids and thinned lamellae were studied using a Zeiss LSM800 upright laser
1241 scanning confocal microscope with a cryostage (Linkam CMS196). Super resolution
1242 images were acquired using a Zeiss 100x air immersion objective (EC Epiplan
1243 NeoFluar, DIC, NA=0.75) and an AiryScan Detector. MCherry-p62 was detected using
1244 a 561nm diode. Image processing was done using Zen Blue (Carl Zeiss GmbH,
1245 version 3.3.89).

Correlative light and electron microscopy

Cryo-lamellae were made in a correlative manner using the in-chamber METEOR fluorescence microscope (Delmic, Cat No 2707-999-0014-2) equipped with a LMPLFLN 50×, NA = 0.5, WD = 10.6 mm objective lens in the Aquilos2 cryo-FIB-SEM system (ThermoFisher Scientific). In short; micropatterned grids with RPE1 cells were loaded under cryogenic conditions taking special care to avoid contamination build-up from air humidity. Cells were located using the electron beam and the sample was placed at eucentric height using MAPS software (ThermoFisher Scientific, version 3.19). Cell phenotype was confirmed by imaging each cell in the METEOR fluorescence microscope. Each cell was imaged using the focused ion beam and the location of the final 150 nm lamella was marked in AutoTEM (ThermoFisher Scientific, version 2.4.1). The lamellae were generated using a step-wise process; the cell was thinned to 1 µm with a 0.5 nA milling current, then thinned to 600 nm with a 0.3 nA current, next to 300 nm with a 0.1 nA current and finally thinned to 200 nm with a 50 pA ion beam. The final polishing step in which the lamella was thinned to 120-180 nm took place with a 30 pA ion beam. The final lamella was once again imaged using the METEOR fluorescence microscope and these images were used to determine where tomograms would be recorded. The lamella were coated with a thin platinum layer; sputtered for 7 seconds at 7 mA, to prevent sample charging. For a more detailed protocol see Berkamp et al. Bio-Protocols 2023 (Berkamp et al., 2023). Next, the samples were transferred under cryo-conditions to a 200 kV Talos Arctica G2 transmission electron microscope (ThermoFisher Scientific), equipped with a Bioquantum GIF (Gatan, Inc) and a K3 direct electron detector (Gatan, Inc). Tilt series were recorded on p62 positive areas of the lamellae, using SerialEM (version 4.2.0)(Mastronarde, 2005) as movies at 24,000x magnification with a 1.7435 Å/pixel size in super resolution mode and a dose of approximately 2.2 e/Å^2/tilt, 10 frames per tilt, and a total dose per tilt series of approximately 130 e/Å^2. All tilt series were recorded from -54° to 54° with 3° increments starting at the pre-tilt of the lamella, using a dose-symmetric bidirectional acquisition scheme with weighted dose according to tilt angle and a nominal defocus of -7 µm. The raw data was motion corrected and CTF corrected using WARP (version 1.0.9) (Tegunov & Cramer, 2019) and the tilt series were reconstructed using Aretomo2 (SBGrid) (Morin et al., 2013; S. Zheng et al., 2022). To aid the cryo tomogram visualization, they were deconvolved, denoised and the missing wedge compensated using IsoNet (Liu et al., 2021) and cryoCARE (Buchholz et al., 2019). To aid in segmentation a pre-trained U-Net model for non-denoised data in MemBrain-Seg (version 9b) (Lamm et al., 2022) was used and the processed tomograms were then loaded into Amira 3D (ThermoFisher Scientific,

version 2022.2) for semi-manual segmentation. Tomograms were visualized using the IMOD software package (version 4.11.20) (Mastronarde & Held, 2017). To aid in targeting the EDX spectra, high dose, single tilt micrographs were recorded on p62 positive areas of the lamellae at 24,000x and a dose of approximately 40 $e^-/Å^2$/micrograph and 180 frames per tilt with each a dose of approximately 0.24 $e^-/Å^2$. Motion correction for these micrographs was done in Relion (SBGrid, version 4.0.1) (Kimanius et al., 2021)

Energy-dispersive X-ray (EDX) spectroscopy

The in situ EDX experiments were carried out on a probe-corrected 200 kV FEI Titan microscope (ThermoFisher Scientific) fitted with a Super-X G2 quadrant detector EDX system (Bruker) and a Simple Origin dual grid cryo transfer holder (Simple Origin, Inc). The microscope was operated under cryo-conditions in STEM mode with a 1.5 mrad convergence angle, a 1 nm probe size at a magnification of 55,000, resulting in a 2.9 nm pixel size. EDX spectra were recorded with a 50 µs dwell time and 50 frames resulting in a total dose of 500 $e/Å^2$, a camera length of 3.5m and a detector dead time of approximately 70%. EDX spectra processing was done in Velox (ThermoFisher Scientific, version 3.14). Atomic map representations were rendered with a 12 px pre-filter average and a 12 px post-filter average for the p62 structures and a 25 px pre-filter average and a 9 px post-filter average for the lipid droplet and lysosome control experiments. The spectra were generated by segmenting the p62 coat in the HAADF-STEM micrograph and segmenting the same number of pixels in the lipid droplet core and a random area of the cytosol. This same process was followed for the control experiments.

Acknowledgements

S.B. was supported by a fellowship from the Alexander von Humboldt Foundation. This work was supported by the European Research Council under Grant Agreement 101118656 (ERC Synergy project 4D-BioSTEM). The work was initially supported by the Boehringer Ingelheim Fonds Exploration grant. The authors would like to thank Andreas Brech and Sebastian Schultz from Oslo University Hospital, Oslo, Norway for providing the stable mCherry-p62 RPE1 cell line. LT acknowledges the support India Alliance DBT/Wellcome trust grant (IA/21/2/505925). The authors gratefully acknowledge the electron microscopy access time and computing time granted by the biological EM facility of the Ernst-Ruska Centre at Forschungszentrum Jülich. In particular, we thank Julio Ortiz for the recording of the Volta phase plate p62 filament tomograms. The authors gratefully acknowledge the computing time granted by the

JARA Vergabegremium and provided on the JARA Partition part of the supercomputer JURECA at Forschungszentrum Jülich (Thörnig, 2021).

Author Contributions

SB, SM, LJ and CS designed the project. SM, AK, LJ purified p62 filaments. SM and AK determined the cryo-EM structure of p62. LJ and AK reconstituted p62 filaments with binding partners and LC3b conjugated liposomes. AK, OK and JF performed single-particle fluorescence measurements and analysis. SB performed the live cell confocal imaging and data analysis. SB performed in situ CLEM followed by cryo-ET analysis. SB, PL and RDB performed the EDX measurements and analus. SB, LJ, AK and CS wrote the manuscript with input from the other authors.

Competing Interest Declaration

The authors declare no competing interests.

Data and code availability

The EMDB accession number for the p62 cryo-EM map is EMD-52134 and the corresponding PDB-ID 9HGE for the fitted PB1 coordinates.